bioRxiv preprint doi: https://doi.org/10.1101/2022.06.27.497721; this version posted June 29, 2022. The copyright holder for this preprint (which was not certified by peer review) is the author/funder. All rights reserved. No reuse allowed without permission.

Granger causality analysis for calcium transients in neuronal networks: challenges and improvements

Xiaowen Chen,[1,2] Faustine Ginoux,[1,3] Thierry Mora,[2,4,5] Aleksandra M. Walczak,[2,4,5] and Claire Wyart[3,4,5]

[1] *These authors contributed equally.*
[2] *Laboratoire de physique de l'École normale supérieure, CNRS, PSL University, Sorbonne Université, and Université Paris Cité, 75005 Paris, France*
[3] *Spinal Sensory Signaling team, Sorbonne Université, Paris Brain Institute (Institut du Cerveau, ICM), Inserm U1127 CNRS UMR 7225; Paris 75013, France.*
[4] *These authors contributed equally.*
[5] *These authors are co-corresponding authors.*

(Dated: June 27, 2022)

A major challenge in neuroscience is to understand how information flows between neurons, triggering specific behaviour. At large scales, Granger causality (GC) has been proposed as a simple and effective measure for identifying dynamical interactions. At single-cell resolution however, GC analysis is rarely used compared to directionless correlation analysis. We discuss here the applicability of Granger Causality analysis for population calcium imaging data. We used recordings from motoneurons in the zebrafish embryo and the entire brainstem region of zebrafish larvae during active visuomotor behavior, and synthetic data simulating intracellular calcium fluctuations of spiking neurons in a chosen neuronal network. We first show that despite underlying linearity assumptions, GC analysis can successfully retrieve non-linear interactions in a synthetic network. We then discuss the potential pitfalls and challenges when applying GC analysis on population calcium imaging data, including the effects of calcium signal preprocessing and motion artefacts. We show how to optimize the choice of GC analysis parameters, such as the relevant time delay and the GC value significance threshold to account for the properties of the data. Applied to motoneuron and hindbrain datasets from larval zebrafish, we show how the improved GG better reflects information flow between neurons.

I. INTRODUCTION

The prompt integration of sensory inputs by motor centers in the nervous systems can become a matter of life and death, often requiring fast and precise movements in response to the stimulus. Understanding how millions of neurons coordinate to generate cognitive activities requires knowing how information from the stimuli flows through networks of neurons to result in the observed behavior. Recent developments in optogenetics [1, 2], and whole-brain imaging with single cell resolution [3–6] allow us to observe collective firing patterns of many neurons and give the basis for reconstructing a causality network that describes how neurons influence each other. However, despite the existing data, assessing the direction of neuronal communication or causality in order to understand how information flows in the brain during integrative reflexive behaviors remains a major challenge in neuroscience [7].

Apart from perturbing individual neurons and observing the activity of downstream neurons, non-invasive methods for obtaining functional connectivity have been developed [8]. The widely used correlation analysis [9–11] identifies pairs or groups of neurons that are active at the same time, suggesting either that they drive each other, or are driven by a common input. By contrast, Granger causality (GC) identifies directed interactions [12–14]. Assuming that the two time-series are well described by Gaussian autoregressive processes, GC quantifies the ability to predict the future values of the time series of a given neuron using prior values of the time series of other neurons. In the field of neuroscience, GC has been used to analyze data from diverse sources [15], including electroencephalography (EEG), magnetoencephalography (MEG) [16], functional magnetic resonance imaging (fMRI) [17–19], and local field potentials (LFP) [20]. Despite criticisms such as sensitivity to data preprocessing [21], internal dynamics of the neuron [22], additive noise [23, 24], and sampling frequency [25, 26], GC and its extensions [27, 28] have been useful to construct functional connectomes, to identify important neurons as information hubs, and to classify different brain states [29].

While most GC analyses in neuroscience focus on large scale ensemble-level neuronal signals, it is unclear how well it can be adapted to address single-cell level descriptions, such as spiking [30, 31] or population calcium imaging data [32–34]. Without the law of large numbers, these single-cell time series are no longer approximately Gaussian, the dynamics of signal propagation is increasingly nonlinear, and the sampling rate is typically much slower than the rate of information propagation. All of these points cast doubt on whether GC can correctly identify information flow. Recently however, De Vico Fallani *et al.* demonstrated in zebrafish embryos that, despite slow sampling frequency of acquisition for calcium imaging (4 Hz), GC can detect information flow consistent with the known rostrocaudal propagation of activity among motoneurons in the spinal cord [32]. Oldfield *et al.* subsequently applied GC to grouped averages

bioRxiv preprint doi: https://doi.org/10.1101/2022.06.27.497721; this version posted June 29, 2022. The copyright holder for this preprint (which was not certified by peer review) is the author/funder. All rights reserved. No reuse allowed without permission.

of calcium signals over entire brain regions, and detected the information flow from the pretectum to the tectum in the visual system leading to the activity of brainstem and motor circuits during prey capture in larval zebrafish [34]. Nonetheless, at the single cell resolution, it is unclear how generalizable the application of GC analysis in population calcium imaging is, and how GC analysis should be improved to accommodate intrinsic features of calcium signals.

In this manuscript, we identify a set of issues inherent to GC analysis when applied to population calcium imaging, using both zebrafish neuronal data and synthetic neural signals as examples, and provide an improved analysis pipeline customized for calcium signals. We address issues specifically related to calcium signals, such as its slow exponential decays, correlated noise, and non-linear and non-Gaussian statistics. We develop our method both on a synthetic network of neurons for which we know the interaction structure, as well as on real data from motoneurons in the embryonic zebrafish spinal cord [32]. We apply our final analysis pipeline to published calcium imaging recordings of the motoneurons of embryonic zebrafish [32] and of the entire brainstem region of larval zebrafish during active visuomotor behavior [33].

II. RESULTS

A. Granger Causality

Granger causality quantifies the ability to predict the future values of the discrete time series of neuron X of length T, $\{x_t\}$, for $t = 1, 2, \ldots, T$, using prior values of the time series of neuron Y, $\{y_t\}$, for $t = 1, 2, \ldots, T-1$, assuming that the two time-series are well described by Gaussian autoregressive processes [12, 15]. The method asks whether including information from Y to predict X has significant predictive power, by computing a p-value assuming as a null model the probability that the dynamics of X can be explained without Y. The prior values of neuron X and Y itself used in that prediction are taken for a finite number of past time points, which defines a characteristic timescale.

With only the information of X itself, the dynamics of X, x_t, may be modeled as an autoregressive process, denoted as the *"reduced model"*,

$$x_t = \widetilde{a}_0 + \sum_{q=1}^{L} \widetilde{a}_q x_{t-q} + \widetilde{\varepsilon}_t, \tag{1}$$

where $\widetilde{a}_q$ are the regression coefficients, the lag L is a hyper-parameter subject to tuning, and $\widetilde{\epsilon}_t$ is a residual term, assumed to be Gaussian.

Alternatively, one can also write down a linear regression model for x_t given the history of both neuron X and neuron Y. This *"full model"* is

$$x_t = a_0 + \sum_{q=1}^{L} a_q x_{t-q} + \sum_{q=1}^{L} b_q y_{t-q} + \varepsilon_t, \tag{2}$$

where a_q and b_q are the regression coefficients for the contribution of neuron X and Y's history to neuron X's current state and ϵ_t is a residual term, also assumed to be Gaussian.

The key idea of Granger causality is to compare the residuals between the reduced and the full models. Intuitively, if neuron Y can influence X, including the dynamics of Y will improve the prediction of x_t, and hence reduce the residual term. As the reduced model is nested within the full model, to test whether the distributions of the residuals, $\{\varepsilon_t\}$ and $\{\widetilde{\varepsilon}_t\}$ are significantly different requires a one-way analysis of variance (ANOVA) test carried out by computing the F-test statistic:

$$F_{\mathrm{Y}\to\mathrm{X}} = \frac{\sum_{t=L+1}^{T} \left(\widetilde{\varepsilon}^2(t) - \varepsilon^2(t)\right) / (M_{\mathrm{f}} - M_{\mathrm{r}})}{\sum_{t=L+1}^{T} \varepsilon^2(t) / (T_{\mathrm{regr}} - M_{\mathrm{f}})}, \tag{3}$$

where $T_{\mathrm{regr}} = T - L$ is the number of time points used in the regression, and $M_{\mathrm{f}} = 2L + 1$ and $M_{\mathrm{r}} = L + 1$ are respectively the number of parameters in the full and reduced models. Under the null hypothesis that including y_t does not improve the prediction of x_t, and that the noise can be described by Gaussian i.i.d., the F-statistics will follow an F-distribution with defined degrees of freedom, $\mathcal{F}(F; M_{\mathrm{f}} - M_{\mathrm{r}}, T_{\mathrm{regr}} - M_{\mathrm{f}})$. Hence, testing the computed F-statistic $F_{Y\to X}$ against the F-distribution will distinguish whether Y significantly Granger-causes X.

To measure the amount of reduction in the residual, the bivariate Granger causality value (BVGC) is defined as

$$GC_{\mathrm{Y}\to\mathrm{X}} \equiv \ln \frac{\mathrm{var}(\widetilde{\varepsilon})}{\mathrm{var}(\varepsilon)} = \ln \frac{\sum_{t=L+1}^{T} \widetilde{\varepsilon}_t^2 / (T_{\mathrm{regr}} - M_{\mathrm{r}})}{\sum_{t=L+1}^{T} \varepsilon_t^2 / (T_{\mathrm{regr}} - M_{\mathrm{f}})}, \tag{4}$$

where the sample variance requires a correction using the number of samples in the regression ($T_{\mathrm{regr}} = T - L$) minus the number of regression parameters (M_{r} or M_{f}). Mathematically, the GC value is related to the F-test statistic through a monotonic transformation:

$$GC_{\mathrm{Y}\to\mathrm{X}} = \ln \left[\left(\frac{M_{\mathrm{f}} - M_{\mathrm{r}}}{T_{\mathrm{regr}} - M_{\mathrm{f}}} F_{\mathrm{Y}\to\mathrm{X}} + 1 \right) \frac{T_{\mathrm{regr}} - M_{\mathrm{f}}}{T_{\mathrm{regr}} - M_{\mathrm{r}}} \right] \tag{5}$$

A significant-only GC value, $GC^{\mathrm{sig}}_{\mathrm{Y}\to\mathrm{X}} = GC_{\mathrm{Y}\to\mathrm{X}}$ is called if the null test of the F-statistics is rejected, and zero otherwise.

In multi-component systems with more than two variables, one needs to consider the influence of other neurons or of a common stimulus, which we collectively denote by $\mathbf{Z} = \{\mathrm{Z}_1, \ldots, \mathrm{Z}_N\}$. For example, to analyze a time series of $N + 2$ neurons $\{x_t, y_t, \mathbf{z}_t\}$, one needs to distinguish direct information flow from Y to X, from indirect information flow from Y to $\mathbf{Z}$ and from $\mathbf{Z}$ to X, or from a

bioRxiv preprint doi: https://doi.org/10.1101/2022.06.27.497721; this version posted June 29, 2022. The copyright holder for this preprint (which was not certified by peer review) is the author/funder. All rights reserved. No reuse allowed without permission.

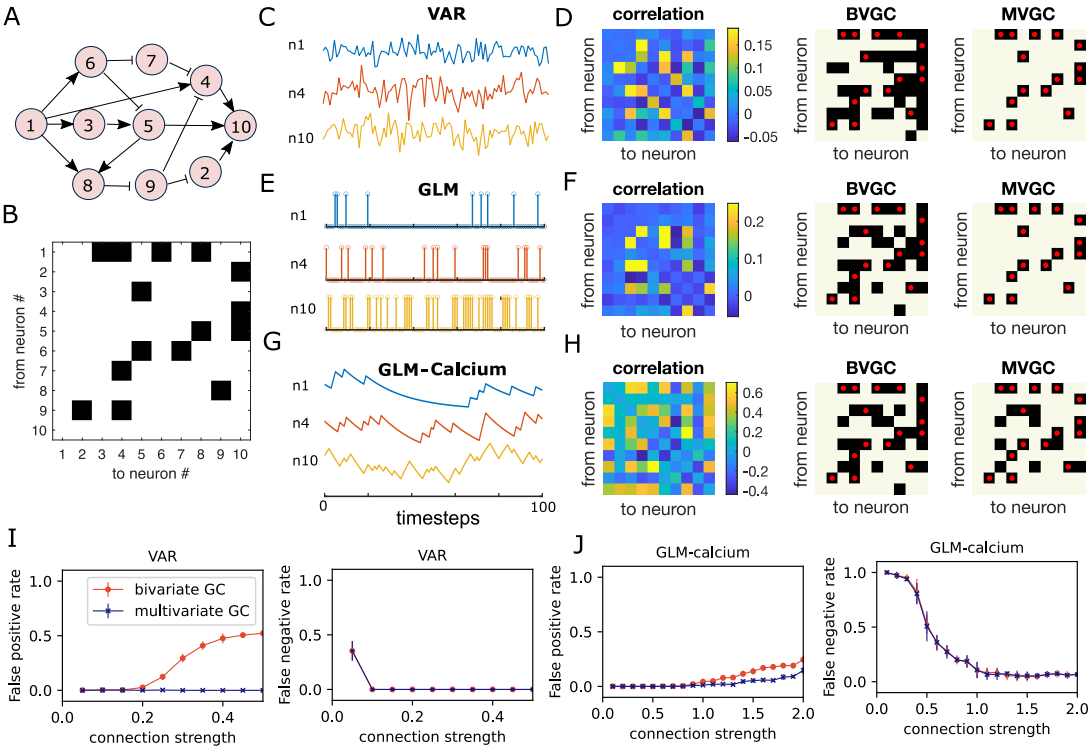

FIG. 1: **Granger causality (GC) analysis on synthetic data generated from 10 interconnected neurons.** (A) The network diagram and (B) the connectivity matrix of the model. The arrows are the excitatory links, and the short bars inhibitory links. Time series are generated and analyzed using correlation analysis and GC, using either a vector autoregressive (VAR) process with connection strength $c = 0.3$ (C-D), a generalized linear model (GLM) with connection strength $c = 1.5$ (E-F), and a GLM with calcium filtering as in the experiments (G-H). (D,F,H) Comparison performance of correlation analysis, bivariate (BVGC) and multivariate (MVGC) GC in predicting the connectivity matrix. True connectivity are indicated with red dots. The error rate of connectivity identification varies as a function of interaction strength c for both the VAR dynamics (I) and the GLM-calcium-regressed dynamics (J). The multivariate GC always does better at predicting true connectivities than the bivariate (pairwise) GC and than correlation analysis.

common but delayed drive from $\mathbf{Z}$ to Y and from $\mathbf{Z}$ to X. Geweke extended Granger causality to a multivariate version (MVGC) to measure the conditional dependence between variables [14]. In this case, we explicitly include the variables describing all possible other neurons and external stimuli, $\mathbf{z}_t = \{z_{1,t}, \ldots, z_{N,t}\}$, as regressed variables in both the reduced model and the full model. The current state of neuron X, x_t, now also depends on the past of $\mathbf{Z}$, such that the reduced and the full models become

$$x_t = \widetilde{a}_0 + \sum_{q=1}^{L} \widetilde{a}_q x_{t-q} + \sum_{j=1}^{N} \sum_{q=1}^{L} \widetilde{c}_{j,q} z_{j,t-q} + \widetilde{\varepsilon}_t, \qquad (6)$$

and

$$x_t = a_0 + \sum_{q=1}^{L} a_q x_{t-q} + \sum_{q=1}^{L} b_q y_{t-q} + \sum_{j=1}^{N} \sum_{q=1}^{L} c_{j,q} z_{j,t-q} + \varepsilon_t, \qquad (7)$$

where $\widetilde{c}_{j,q}$ and $c_{j,q}$ are the regression coefficients from the conditioned signal z_j. The F-test statistics $F_{\mathrm{Y}\to\mathrm{X}|\mathbf{Z}}$ and the GC values $GC_{\mathrm{Y}\to\mathrm{X}|\mathbf{Z}}$, have identical expression as in Eq. (3) and Eq. (4), with the number of parameters in the reduced and the full model adjusted accordingly.

It is important to point out that, although GC is based on linear regression of time series, its use is not limited to data generated by linear dynamics. In fact, as long as the data can be approximated by a vector autoregressive process, GC can be useful in revealing the information flow [15]. For analysis of calcium signals, the intrinsic nonlinearity of calcium decay means it is not obvious *a priori* whether GC can be useful in revealing the information structure. As we will show in the following, the success of information retrieval depends on the details of the biological network, such as the interaction strength between pairs of neurons and the connection density, which leads to a complicated interplay among different timescales, such as the firing rate, the calcium decay time constant, and the time scale of information transfer.

bioRxiv preprint doi: https://doi.org/10.1101/2022.06.27.497721; this version posted June 29, 2022. The copyright holder for this preprint (which was not certified by peer review) is the author/funder. All rights reserved. No reuse allowed without permission.

B. GC analysis of a small synthetic neuronal net

To gain some intuition about how GC identifies links, we test it on synthetic data generated using small networks of 10 neurons, where we pre-define the true connectivity (Fig. 1A and B). One of the simplest types of dynamics is given by the same model that underlies the GC analysis, the vector autoregressive model (VAR), where the neural activities $f_{i,t}$ evolve according to

$$f_{i,t} = \sum_{q=1}^{L_{\text{true}}} \sum_{j} \Gamma_{ij,q} f_{j,t-q} + \xi_{i,t}, \tag{8}$$

where $\Gamma_{ij,q}$ is a memory kernel capturing the effect from neuron j at time $t-q$ on neuron i at time t, and $\xi_{i,t}$ a Gaussian noise with zero mean and variance σ^2. For simplicity, we assume the memory kernel acts only within the preceding two time steps, $L_{\text{true}} = 2$, and set $\Gamma_{ij,q} = A_{ij} s_j c$ for $q \leqslant L_{\text{true}}$, and zero, otherwise. A_{ij} is the adjacency matrix: $A_{ij} = 1$ if neuron j is directly presynaptic to neuron i, and $A_{ij} = 0$ otherwise. The sign of interaction s_j shows whether neuron j is excitatory ($s_j = 1$) or inhibitory ($s_j = -1$). To ensure that the synthetic time series is stationary, we set the number of excitatory cells and inhibitory cells to be equal, and accordingly choose a positive interaction strength c. The simulation time step is set as the unit time, $\Delta_{\text{sim}} = 1$.

We apply the GC analysis to synthetic data generated using the VAR model (Fig. 1C) to see if we can recover the true network connectivity. For each neuron pair (i, j), we compute the BVGC values following Eq. 4, identifying $x_t = f_{i,t}$ and $y_t = f_{j,t}$, and computing the regression coefficients a_q and b_q using the standard least squares method. Analogously, we also compute the MVGC values, using all the remaining neuron signals $f_{k,t}|_{k \neq i,j}$ as the conditional variables $\boldsymbol{z}_t$.

As shown in Fig. 1D, MVGC successfully identifies all the links. However, the bivariate GC assigns spurious links, as it cannot distinguish direct links from indirect ones. In general, MVGC has a lower false positive rate (identified non-existing links) and false negative rate (missing true links) compared to BVGC when we vary the connection strength c (Fig. 1I). It is interesting to point out that, at small connection strengths, both MVGC and BVGC will fail to identify true links because the signal-to-noise ratio is too small to detect them. In comparison to both GC analyses, the equal-time correlation completely misses the structure (see Fig.1D and **Materials and Methods**). While cross-correlation with the lag fixed to the model lag L_{true} performs better, it still fails to reproduce the true connectivity as faithfully as MVGC (see Fig. S1).

To gain intuition if GC can work for more realistic single-neuron dynamics, which are typically very different from the linear VAR model, we perform the same analysis with dynamics generated with generalized linear models (GLM). We assume the spike count of neuron i at time t, $\sigma_{i,t} \sim \text{Poiss}(\lambda_{i,t})$ is governed by a Poisson process with spiking rate $\lambda_{i,t}$

$$\lambda_{i,t} = \exp\left(\mu_i + \sum_{q=1}^{L_{\text{true}}} \sum_{j} \Gamma_{ij,q} \sigma_{j,t-q}\right), \tag{9}$$

where μ_i is the base rate for spiking, and the memory kernel $\Gamma_{ij,q}$ is identical to the VAR model. We can further regress the spikes with an exponential decay function to simulate calcium signals (GLM-calcium) (see **Materials and Methods** for details).

Although the GLM and GLM-calcium dynamics are highly non-linear and non-Gaussian (Fig. 1E and G), MVGC successfully identifies true links (see Fig. 1FGJ). In general, for large correlation strengths, the false negative rate (missing true links) is less than 0.1. Interestingly, for the GLM-calcium model, the false positive rate (identified non-existant links) at large connection strength is smaller than in the VAR model, as is the difference of errors between the MVGC and BVGC. A possible explanation is that for neurons with nonlinear interactions, the propagation of information in indirect links is less well described by linear models in direct links. In comparison, due to large auto-correlation caused by decay of the calcium signal, the correlation and cross-correlation performs much worse for the nonlinear dynamics than for the VAR model (see Fig. S2 and S3).

This analysis of synthetic data shows that GC can reveal underlying connectivity structures from calcium signals, and that the performance difference between BVGC and MVGC is smaller in nonlinear models.

Time lag. In GC analysis, it is essential to choose the time lag L. If the time lag L is much less than the true interaction timescale L_{true}, then the reconstructed information flow will be incomplete. On the other hand, if L is too large, we will run into the risk of overfitting [15]. Here, we briefly discuss the effect of the lag L on the resulting GC network, using data generated by the synthetic network given by Fig. 1A, simulated with VAR dynamics with true lag $L_{\text{true}} = 3$.

As we vary L, the time lag used in the GC regression models, we observe that increasing the time lag does not always improve our ability to identify the network connectivity (Fig. 2FG). Going beyond the true time lag leads to errors, increases both the false positive rate (Fig. 2F) and the false negative rate (Fig. 2G). Compared to MVGC, BVGC is more prone to detect spurious links, even at the correct time lag.

Interestingly, we observe that the average GC value as a function of the number of lags can be used to identify the true time lag L_{true}. As shown by Fig. 2H, both the average BVGC and MVGC values increase steeply as L approaches the true lag, and reach a plateau for a few lag values before overfitting significantly increases the average GC values. Based on this observation, we select the time lag to be the knee of the average GC value as a function of the lag, as this time lag captures enough in-

bioRxiv preprint doi: https://doi.org/10.1101/2022.06.27.497721; this version posted June 29, 2022. The copyright holder for this preprint (which was not certified by peer review) is the author/funder. All rights reserved. No reuse allowed without permission.

formation flow while the number of fitted parameters is kept as small as possible.

C. GC analysis of motoneuron data

1. The data

In order to test the performance of Granger causality on population calcium imaging data, we focus our analyses on previously published calcium transients in motoneurons of embryonic zebrafish (*Tg(s1020t:Gal4; UAS:GCaMP3)*, data published in [32]). The calcium transients were recorded using fluorescent tags *in vivo* for 250s at 4Hz and with single-cell resolution, in ventral spinal cord motoneurons while the zebrafish was showing spontaneous coiling activity of its tail (Fig. 2A–C). During these fictive coiling events, the activity of motoneurons follows a wave from the rostral to the caudal side of the spinal cord [35–37]. Upon activation along the rostrocaudal axis, spinal motoneurons that project to the axial skeletal muscle fibers elicit a rostrocaudal wave of muscle contractions that alternates between the left and right side of the body and propels fish forward. Accordingly, the calcium signals show steady oscillations alternating between the left and right sides of the spinal cord, leading to left-right muscle activation (Fig. 2C). We use this data set in order to see if we recover the expected sequential information flow, from the rostral spinal cord to the caudal spinal cord (arrows in Fig. 2A, networks in Fig. 2D).

To encode the underlying information structure of the neuronal network, we label the recorded N neurons with index i, and the side of the neurons by $s_i \in \{\mathrm{L}, \mathrm{R}\}$. Assume that there are N_l neurons in the left chain and N_r neurons in the right chain, we order the indices such that the odd neurons are found on the left side, with $s_i = \mathrm{L}$ for $i = 1, 3, \ldots, 2N_l - 1$, and the neurons with $i = 2, 4, \ldots, 2N_r$ are found in the right chain with $s_i = \mathrm{R}$. The indices are then ordered by the neurons position along each of the two chains, such that if $s_i = s_j$, neuron i is more rostral than neuron j if $i < j$. The fluorescence signal for the i-th cell at time t is denoted by $f_i(t)$, or equivalently by $DF_i/F_i(t)$ to represent the normalized fluorescence activity.

We will compute the GC network for multiple trials of calcium transients recorded in 5 fishes. Following the nomenclature of the dataset published by [32], we refer to the dataset recorded for fish A and trial B as $fAtB$; for example, $f3t2$ denotes trial number 2 recorded for fish number 3.

2. Naive GC

We apply the GC algorithm as described in Section II A to the calcium transients observed in embryonic motoneurons, and reproduce the results obtained in [32] for the dataset *f3t2*. We choose the time lag at the knee of average GC value, $L = 3$, corresponding to a lag of 750ms, for both BVGC and MVGC analysis (Fig. 2I). The GC network is then represented by directed graphs (Fig. 2E). The nodes of the graph represent the motoneurons and the circle size is proportional to the *nodal delta centrality* as defined by [32]: the larger the circle, the more central is the neuron in terms of its tendency to act as a transmitter hub (red color, positive value) or receiver hub (blue color, negative value) of information flow. Arrows display the functional connectivity links, i.e. the flow of information from one neuron to another. In the expected network assuming perfect information flow (Fig. 2D), all the links are ipsilateral and represent rostrocaudal information flow.

Compared to [32], we identify the same functional connectivity matrices yielding the same connectivity networks. While the previous study focuses on recovering ipsilateral links and ignores contralateral links (depicted in dim gray in the network figures, see [32]), we investigate all contralateral links and ipsilateral links (Fig. 2E) as we aim to study why spurious contralateral connections occur. We represented the statistically significant direct GC links by arrows, proportional in size and color intensity to the GC value. The networks resulting from the GC analyses both for BVGC and MVGC show many other links than just rostrocaudal ones on either side.

In the MVGC analysis however, one would have expected only direct links to be significant, since conditioning on the other neuronal signals should prevent indirect links from being significant. This expectation is very different from the MVGC network in Fig. 2E, where spurious contralateral links prevails. Nonetheless, it is well known that MVGC is sensitive to additive noise, lack of data points, etc. To assess the impact of these artifacts on the resulting GC networks for motoneuron data, we define measures of information flows as following.

3. Defining directional biases

To quantify the success of reconstructing the information flow in the motoneuron network, and to compare the information flow across different datasets, we define the following measures of directional biases. First, we define the ratio of normalized total weights of ipsilateral links compared to all links

$$W_{\mathrm{IC}} = \frac{\langle G_{ij} \rangle_{(i,j)|s_i=s_j}}{\langle G_{ij} \rangle_{(i,j)|s_i=s_j} + \langle G_{ij} \rangle_{(i,j)|s_i\neq s_j}}, \qquad (10)$$

where G_{ij} is the Granger causality values between neurons i and j. If all connections are equal, then $W_{\mathrm{IC}} = 0.5$.

bioRxiv preprint doi: https://doi.org/10.1101/2022.06.27.497721; this version posted June 29, 2022. The copyright holder for this preprint (which was not certified by peer review) is the author/funder. All rights reserved. No reuse allowed without permission.

We also define the ratio of ipsilateral rostral-to-caudal links compared to all ipsilateral links as

$$W_{\mathrm{RC}} = \frac{\langle G_{ij} \rangle_{i<j|s_i=s_j}}{\langle G_{ij} \rangle_{i<j|s_i=s_j} + \langle G_{ij} \rangle_{i>j|s_i=s_j}}. \quad (11)$$

This ratio gives a measure of the directionality of information flow. A bias in rostrocaudal links results in a departure from $W_{\mathrm{RC}} \sim 0.5$. With the two measures of directional biases of information flow, now we proceed to develop an improved pipeline for GC analysis. Using different datasets of the embryonic motoneurons as examples, we will show how to improve GC to analyze calcium transients of neuronal populations. Our goal is to recover a more biologically reasonable information flow compared to the naive GC network.

4. *Correcting for motion artifacts*

In calcium imaging experiments, small movements of the animal body or the experimental setup can result in artificial fluorescence changes in the recording. In the calcium transients of data *f3t1*, we observe a big drop in fluorescence at a single time point out of 1000 (Fig. 3B top panel) in the calcium traces of all neurons in the recording. As seen in the top panels of Figure 3C, this is sufficient to corrupt the results of the GC analyses: neuron 10 (Figure 3A) appears to drive almost all other neurons, including contralateral neurons. We correct the motion artifact by setting the outlying time point's fluorescence value to the average of the previous and next values (Fig. 3B bottom panel). The strongly dominant drive by neuron 10 disappears (Fig. 3C bottom panels) and W_{IC} increases from 0.39 to 0.66 for BVGC and from 0.43 to 0.68 for MVGC (Table 1). This shows that GC analysis is sensitive to artifacts at single time points.

The motion artifact is a global noise on the observed neurons, a source that is well-known to create spurious GC links [23, 24]. After careful examination of the calcium traces, we notice that the dominant neuron before motion-artifact correction, neuron 10, is characterized by its small dynamic range. Because the rest of the activity is low for neuron 10 and that a single time point seems to have a strong effect on other calcium traces, GC links driven by this neuron are high. We looked at other recordings containing a motion artifact and found that removing it did not always eliminate the spurious dominant neurons. The larger the artifact, the better we eliminate the spurious links: in Fig. 3, the artifact represents a deviation of about 80% of the DF/F and its impact on GC links is large. When the deviation is lower, the strong spurious links are not necessarily due to the motion artifact, therefore removing the artifact does not improve the expected network results.

	BVGC		**MVGC**	
	W_{IC}	W_{RC}	W_{IC}	W_{RC}
Before MA correction	0.39	0.53	0.43	0.52
After MA correction	0.66	0.56	0.68	0.44

TABLE 1: The directional measures for the bivariate and multivariate GC network for the calcium transients *f3t1* before and after motion-artifact correction, a pre-processing step for calcium signals. The GC network after motion artifact correction has clear ipsilateral structures.

5. *Removing strange neurons*

In order to improve the GC analysis results, we want to keep only clean calcium signals and remove the traces of uncharacteristically behaving neurons whose activity does not seem relevant for the considered task. This is especially important for the MVGC analysis, in which traces of all other neurons are considered in the calculation of a GC value between two given neurons.Although BVGC values are not affected by neurons outside of the observed pair, having extra neurons might also influence the network structure through the GC values of the links. Since embryonic motoneurons exhibit oscillatory neuronal activity [38], we remove neurons whose trace do not show such characteristic patterns. In the embryonic zebrafish traces *f5t2*, shown in Fig 3E, we remove neuron 13 (Fig. 3D) that displays only one long calcium transient lasting for tenths of seconds, and neuron 21, which does not exhibit an oscillating pattern.

GC networks are drawn for the neuronal populations before (Fig. 3F top panels) and after removal of these outlier neurons (Fig. 3F bottom panels). Before the removal, neuron 21 appears to drive many other neurons, likely due to its lower signal-to-noise ratio (SNR) and the correlated noise between calcium traces. Once removed, W_{RC} increases, meaning that a mostly rostrocaudal propagation is observed, as information in motoneurons flows from the rostral to the caudal spinal cord (Table 2). We also observe a small decrease in W_{IC} upon removal of neuron 21, due to the fact that the ipsilateral links going out from neuron 21 are not present anymore, but spurious contralateral links remain.

	BVGC		**MVGC**	
	W_{IC}	W_{RC}	W_{IC}	W_{RC}
With strange neurons	0.56	0.51	0.59	0.38
Without strange neurons	0.54	0.67	0.53	0.53

TABLE 2: The directional measures for the bivariate and multivariate GC network for the calcium transients *f5t2* before and after removal of the atypical neurons.

bioRxiv preprint doi: https://doi.org/10.1101/2022.06.27.497721; this version posted June 29, 2022. The copyright holder for this preprint (which was not certified by peer review) is the author/funder. All rights reserved. No reuse allowed without permission.

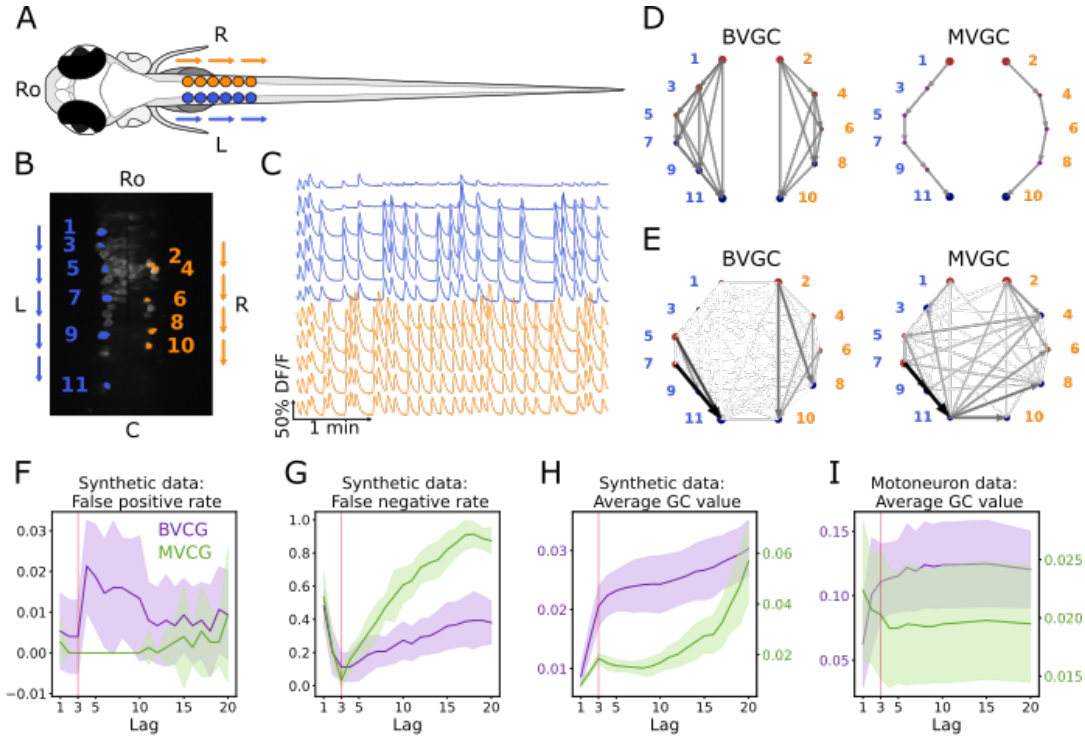

FIG. 2: **Bivariate and multivariate GC analyses of motoneuron calcium imaging recordings in a zebrafish embryo do not match expected ipsilateral and rostral to caudal information flow.** (A) Dorsal view of the embryonic zebrafish and positions of the left (L) and right (R) motoneurons targeted in calcium imaging (colored circles). The arrows represent the wave of activity, propagating ipsilaterally from the rostral (Ro) spinal cord to the caudal (C) spinal cord [32, 35–37]. (B) Mean image of a 30-somite stage embryonic zebrafish (*Tg(s1020t:Gal4; UAS:GCaMP3)*, dataset *f3t2* in [32]), with motoneurons selected for analysis shown in color. (C) Fluorescence signals (proxy for calcium activity) of selected neurons. We observe an oscillating pattern of activation of the left vs right motoneurons. (D) Representation of the motorneuron flow of information as a directed graph as would be ideally defined by bivariate (left) and multivariate (right) GC analyses. (E) Resulting directed networks for bivariate (left) and multivariate (right) GC analyses of fluorescence traces of (C) at lag 3: we observe different networks than expected, both for BVGC and MVGC. (F) Effect of the lag on the False Positive Rate, i.e. the proportion of spurious positive links over all negative links, on synthetic data (VAR) with a true lag of 3, for BVGC (purple) and MVGC (green). BVGC is more prone to detect spurious links, even at the correct lag. This is consistent with the network observed in (E). (G) The False Negative Rate, i.e. the proportion of missed positive links over all positive links, is very sensitive to the choice of the lag. If the chosen lag is very different compared to the true lag, many links will not be detected. Effect of the lag on the average GC values for synthetic (H) and real motoneuron (I) data. Using the average GC value, we choose a lag of 3 for the motoneuron data analysis, corresponding to 750 ms.

6. *Smoothing*

One known limitation of traditional Granger causality analysis is its sensitivity to noise, especially correlated noise across variables [23, 24]. In empirical calcium imaging data, correlated noise is common due to system-wise measurement noise and spurious correlations coming from the slow sampling rate.

To illustrate the problem of the noise, we return to the synthetic models in Section II A, a simulated system of 10-neurons with the VAR and the GLM-calcium dynamics, where the true underlying signal is $f_i(t)$, for each neuron i. We add a system-wide noise, such that the noise-corrupted signal is

$$g_i(t) = f_i(t) + \zeta(t), \tag{12}$$

and $\zeta(t)$ is Gaussian white noise, with $\langle \zeta(t) \rangle = 0$, and $\langle \zeta(0)\zeta(t) \rangle = \sigma_\zeta^2 \delta(t)$. As shown in Figs. S4 and S5, large correlated noise significantly decreases the ability of the Granger causality analysis to identify true connections.

We exploit the stereotypical shape of calcium signals – a fast onset and a slow decay – to parametrize the structure of the noise for empirical calcium signals. We assume that any correlation in the decay phase is the correlation of the noise. Additionally, we apply *total variation regularization* to denoise the fluorescence time series for each neuron [39] (see **Materials and Methods** and Ref. [40] for details). Briefly, for each neuronal signal $f(t)$, total variation regularization assumes the noise is Gaussian and white, and that the temporal variations in the derivative are exponentially distributed and only weekly correlated in time, which is well-suited to describe calcium data with episodes of continuous firing and con-

bioRxiv preprint doi: https://doi.org/10.1101/2022.06.27.497721; this version posted June 29, 2022. The copyright holder for this preprint (which was not certified by peer review) is the author/funder. All rights reserved. No reuse allowed without permission.

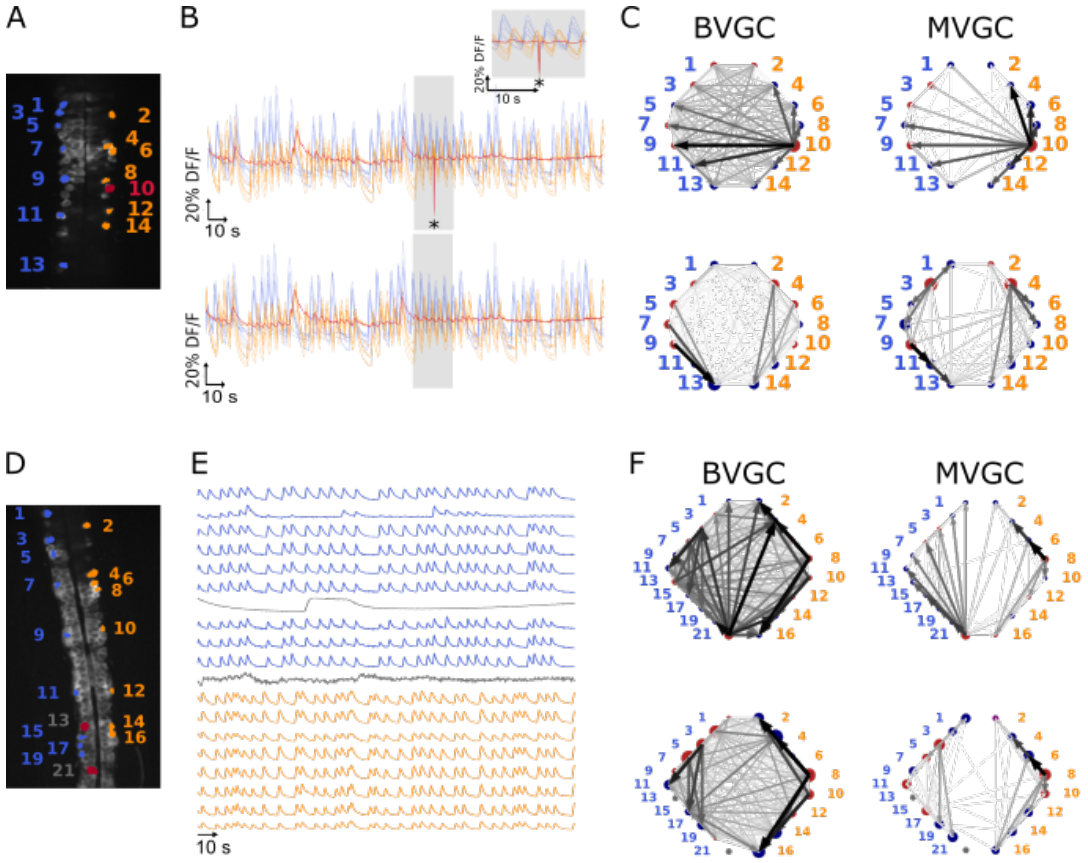

FIG. 3: **One time-point artifact or one noisy neuron fluorescence trace is sufficient to corrupt the GC algorithm.** (A) Mean image of a 30-somite stage larval zebrafish (*Tg(s1020t:Gal4; UAS:GCaMP3)*, dataset *f3t1* in [32]), with neurons selected for analysis shown in color. (B) Fluorescences traces of neurons of (A). Top: A motion artifact consisting of a drop in fluorescence at a single time point is present (star). Bottom: the motion artifact is corrected as being the mean of the two surrounding time points. (C) Directed graph resulting from the bivariate (left) and multivariate (right) GC analysis, before (top) and after (bottom) motion artifact correction. Before the correction, the neuron with the smallest activity appears to drive many other neurons, perhaps due to its lower SNR. This spurious dominant drive disappears once the motion artifact is corrected, demonstrating that GC is not resilient to artifacts as small as one time point out of one thousand. (D) Mean image of a 30-somite stage larval zebrafish (*Tg(s1020t:Gal4; UAS:GCaMP3)*, dataset *f5t2* in [32]), with neurons selected for analysis shown in color. The fluorescence traces (E) of neurons displayed in red exhibit activity patterns different from the oscillatory pattern expected in motorneurons. GC analysis was run after removal of these neurons. (F) Directed graph resulting from the bivariate (left) and multivariate (right) GC analysis, before (top) and after (bottom) removing neuron 13 and neuron 21.

tinuous silence. As an example, Fig. 4A shows the original and the smoothed fluorescence signal for two neurons in the same fish (dataset *f3t2* from [32]), as well as the residual noise. The noise in the motoneuron is correlated with correlation coefficients close to 1 for some pairs of neurons (Fig. 4B). The large correlated noise is likely the cause of our problematic results in the MVGC analysis (see Fig. 2E and Fig. 4C).

Denoising the calcium time series before the GC analysis eliminates links, especially in the MVGC approach (Fig. 4C). The signal as quantified in terms of the relative weight of ipsilateral links W_{IC} is also closer to the biological expectation ($W_{\mathrm{IC}} \sim 1$) than before smoothing, with MVGC giving better results (Fig. 4D).

We note that total variation regularization is a global denoising method that acts on the entire time series. Different from a low-pass filter, total variation regularization is able to keep the fine structure of the fast rise in the calcium signal, while smoothing out the noise. Nonetheless, the assumption is that the noise is Gaussian, which should be verified before smoothing the data by examining the high-frequency end of the signal's power spectrum. To address the problem of high-frequency correlated noise, one may propose to use spectral Granger causality [13, 14], and only focus on the resulting GC values at low frequencies. However, we show that spectral GC applied to the unsmoothed calcium signal is unable to recover the information flow for any of the frequencies (Fig. S6). Finally, in cases where correlated noise cannot be removed, there are alternative methods to reject

bioRxiv preprint doi: https://doi.org/10.1101/2022.06.27.497721; this version posted June 29, 2022. The copyright holder for this preprint (which was not certified by peer review) is the author/funder. All rights reserved. No reuse allowed without permission.

false links, e.g. using Granger causality computed on the time-reversed data as the null hypothesis [24].

7. *Slow calcium timescale*

One potential pitfall of performing Granger causality analysis on single-cell calcium signals is that the timescale of the calcium indicator and the sampling are typically much slower than that of the information transfer. The onset of calcium signals can occur in few milliseconds, comparable with the timescale of information transfer. Nonetheless, based on the intrinsic buffer capability of neurons and the fluorescent properties of the calcium indicator, calcium signals typically decay on the timescale of hundreds of milliseconds to seconds [41]. In motoneurons, neurons can fire in bursts of spikes, which may further hinder the resolution of information propagation. In this section, we investigate how the interplay of these slow and fast timescales impacts the accuracy of Granger causality analysis to identify information flow.

In the embryonic spinal cord, motoneurons are recruited along the rostrocaudal axis sequentially. The muscle contractions alternate between the left and right side of the body, and propel fish forward. Correspondingly, the left and right sides of the motoneurons are active as a steady oscillation from the head to the tail, leading to an expected information flow from caudal to rostral [37]. The spikes are followed by a plateau that lasts on the order of seconds [38]. Using a combined statistical and dynamical approach, we simulate artificial "motoneuron" data (see example traces in Fig. 5A), as two chains of five neurons, driven externally by two binary stimuli, $I_{\mathrm{L}}(t)$ and $I_{\mathrm{R}}(t)$, that randomly flip between an on ($I = 1$) and an off ($I = 0$) state, following the same statistics as recorded in the data. The stimulus of the left side, $I_{\mathrm{L}}(t)$ is generated by randomly choosing time intervals when the stimulus state is on, τ_{on}, and when it is off, τ_{off}, uniformly from the sets $\left[\min(\tau_{\mathrm{on}}^{\mathrm{data}}), \max(\tau_{\mathrm{on}}^{\mathrm{data}})\right]$ and $\left[\min(\tau_{\mathrm{off}}^{\mathrm{data}}), \max(\tau_{\mathrm{off}}^{\mathrm{data}})\right]$, respectively. Here, $\{\tau_{\mathrm{on}}^{\mathrm{data}}\}$ is the set of duration of all "on"-states in the experiment [32] that we find by the positive finite difference method in the fluorescent signal smoothed by total-variational regularization [39, 40]. These sets of long-lasting time blocks, where the neurons are always active, simulates the plateau activity of the embryonic motoneurons. After $I_{\mathrm{L}}(t)$ is sampled, the stimulus for the right-side neurons, $I_{\mathrm{R}}(t)$, is generated such that the time delay between the "on"-state of $I_{\mathrm{L}}(t)$ and $I_{\mathrm{R}}(t)$ is sampled from $\left[\min(\tau_{\mathrm{delay}}^{\mathrm{data}}), \max(\tau_{\mathrm{delay}}^{\mathrm{data}})\right]$, where the delay time τ_{delay} matches the empirical stimulus distribution. We model the sequential activation of the motoneurons by imposing the spike rate as a function of $I_{\mathrm{L}}(t)$ and $I_{\mathrm{R}}(t)$ (see **Materials and Methods**) and we use a standard Poisson process with these rates to generate the spike train for each neuron, $\{\sigma_{i,t}\}$. The spikes is then convoluted with an exponential decay with time scale τ_{ca} to simulate the slow decay time of calcium signals.

The timescales in this model include the sampling time τ_{sampling}, the calcium decay time constant τ_{ca}, and the timescale of information propagation τ_{info}. The sampling time is given by the experimental setup for the motoneuron data we analyze [32], with $\tau_{\mathrm{sampling}} = 0.25\mathrm{s}$. As shown in Fig. S7, the empirical calcium decay time constant can be found by overlaying all epochs of decays of the calcium signals from different bursts and different neurons: fitting the decay of calcium signals to exponential functions gives $\tau_{\mathrm{ca}} = 2.5\mathrm{s}$. Notice this decay timescale is limited by both the buffering capability of the sensor, here GCaMP3, and the intrinsic buffering capability of the cell [41], i.e. having a faster sensor does not always decreases this decay time scale. The information propagation timescale is chosen such that $\tau_{\mathrm{info}} < \tau_{\mathrm{sampling}}$. The basal spike rate is set to $\lambda_0 = 32\mathrm{s}^{-1}$. Finally, the time resolution for the simulation is chosen to be $\Delta_{\mathrm{sim}} = 0.0125\mathrm{s}$, such that $\lambda\Delta_{\mathrm{sim}} < 1$ to add stochasticity in the simulation.

Applying bivariate and multivariate GC analysis to the simulated data with the above parameters, we see that when the information propagation time scale is similar to the sampling time scale, both GC methods retrieve the correct information flow (Fig. 5B). In general, multivariate GC performs better in identifying information flow compared to bivariate GC. Even when the information propagation time scale is much smaller than that of the sampling rate ($\tau_{\mathrm{info}} \leq \tau_{\mathrm{sampling}}$), the information flow can still be correctly retrieved, and the multivariate GC gives the correct input W_{ipsi} value 1, and W_{RC} significantly larger than the null value of 0.5.

The success of retrieval of information flow also depends on the decay constant, although the effect is not strong. As shown in Fig. 5C, the performance is almost perfect for short calcium decay times, with $W_{\mathrm{IC}} = 1$ and $W_{\mathrm{RC}} = 1$, and longer decay result in slightly worse performance. For the empirical calcium decay rate in the GCaMP3-expressing motoneuron data (indicated by the red line), $W_{\mathrm{RC}}^{\mathrm{MVGC}} = 0.81$. Naturally, using fast calcium indicators in the experiments facilitates the analysis, but the improvement may not be significant.

8. *Adaptive threshold for F-statistics*

We now compute the Granger causality strength (Eq. 4) on the smoothed calcium time series. Naively, the F-test is used to determine whether the Granger causality is significant (Eq. 3). This test is exact if the residual, or the prediction error, is Gaussian-distributed and independent. For calcium signals, these assumptions do not hold: the noise is not necessarily Gaussian, and is not independent. To test if we can still use the F-test as a test of significance, we generate data consistent with a null hypothesis by cyclically shuffling the time series of the driving neuron j (see Fig. 6A). Specifically, for the bivariate GC value from neuron j to another neuron i,

bioRxiv preprint doi: https://doi.org/10.1101/2022.06.27.497721; this version posted June 29, 2022. The copyright holder for this preprint (which was not certified by peer review) is the author/funder. All rights reserved. No reuse allowed without permission.

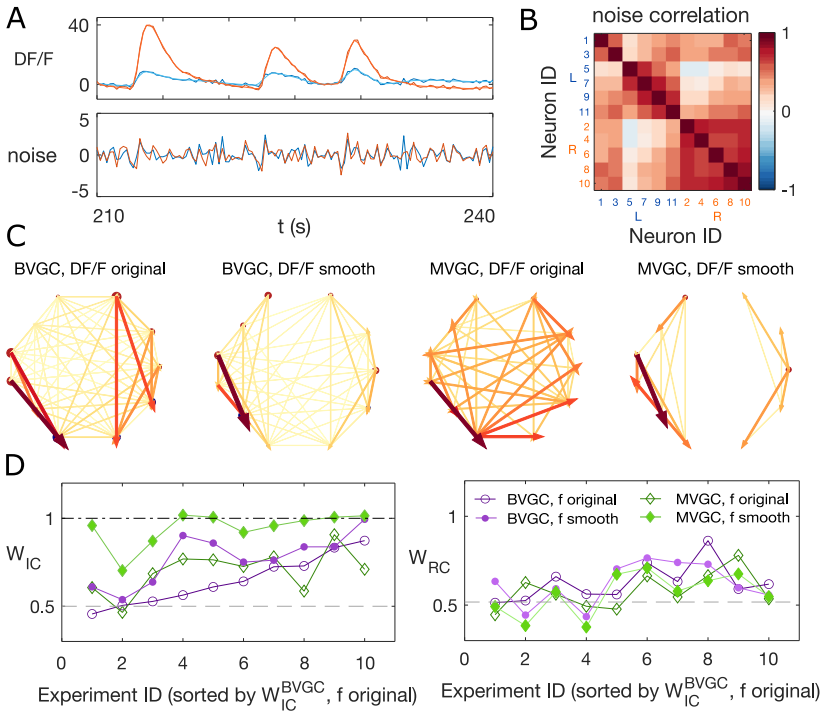

FIG. 4: **Smoothing the calcium imaging signal can improve the accuracy of GC.** (A) We smooth the noisy calcium imaging signal $f = DF/F$ using total-variational regularization (see **Materials and Methods**), and plot the example traces of the original and the smoothened neuronal signals, and the residual noise, using the dataset *f3t2* from [32]. (B) The Pearson correlation coefficient shows the residual noise is correlated. (C) GC networks constructed using the original noisy calcium signal compared to ones using the smoothed signal for motorneurons. (D) Weight of ipsilateral GC links, W_{IC}, and the weight of rostal-to-cordal links, W_{RC}, for the original calcium signals and smoothened signals. We expect $W_{\mathrm{IC}} \sim 1$ and a null model with no bias for where the links are placed will have $W_{\mathrm{IC}} = 0.5$. The x-axis is sorted using the W_{IC} value for bivariate GC analysis with the original calcium data. Data points are connected with lines to guide the eye. The bivariate GC results are plotted with purple circles, and the multivariate GC results with green diamonds. GC analysis results using the original noisy fluroscence signals are shown with empty markers, while the results from first smoothed data are shown with filled markers.

$GC_{j\to i}$, and the multivariate $GC_{j\to i|\{k\}}$ conditioned on the activity of the rest of neurons $\{f_k\}$, $k \neq i, j$, we compute the F-statistics with the time series $f_j(t)$ replaced by signal shuffled by a random time constant Δt^{rand}:

$$f_j^{\mathrm{CS}}(t) = \begin{cases} f_j(t - \Delta t^{\mathrm{rand}}), & 0 < t < T - \Delta t^{\mathrm{rand}} \\ f_j(t + T - \Delta t^{\mathrm{rand}}), & T - \Delta t^{\mathrm{rand}} < t < T \end{cases}. \tag{13}$$

If the significance test remains valid for the calcium time series, we expect almost no significant links and the distribution of the F-statistics of the shuffled data should be the F-distribution. However, as Fig. 6BC shows using the example dataset *f3t2* from [32], for both bivariate and multivariate GC, the distribution of the F-statistics for the shuffled data, $\mathcal{F}^{\mathrm{shuffle}}$, has a shifted support that is larger than that of the F-distribution. This means that if we use the original F-test based on the F-distribution as a null model, even if there are no G-causal links between two neurons, we will classify the link as significant.

To improve specificity, we instead define the null expectation as the distribution for the F-statistics of the cyclically shuffled data to test for the significance of GC links. A GC link from the data is significant, if it has an F-statistics that is above the $1-p$ percentile of the null F-statistics distribution, generated from the cyclically shuffled data. The null F-statistics distribution can be approximated non-parameterically by Monte Carlo reshuffles. However, since the significance threshold depends on the tail of the F-statistics distribution, to get an accurate estimation requires a large number of reshuffles and is computationally undesirable.

Instead, to accelerate the computation, we notice that the bulk of the $\mathcal{F}^{\mathrm{shuffle}}$ distribution is well approximated by an F-distribution, with outliers explained by the pseudo-periodicity of the data. We parameterize the null empirical distribution by $\mathcal{F}(F; \alpha, \beta)$, and find the parameters by maximizing the likelihood (see **Materials and Methods** for details). Repeating the significance test with the parametrized F-distribution, we find a resulting causality network with fewer links (Fig. 6D).

bioRxiv preprint doi: https://doi.org/10.1101/2022.06.27.497721; this version posted June 29, 2022. The copyright holder for this preprint (which was not certified by peer review) is the author/funder. All rights reserved. No reuse allowed without permission.

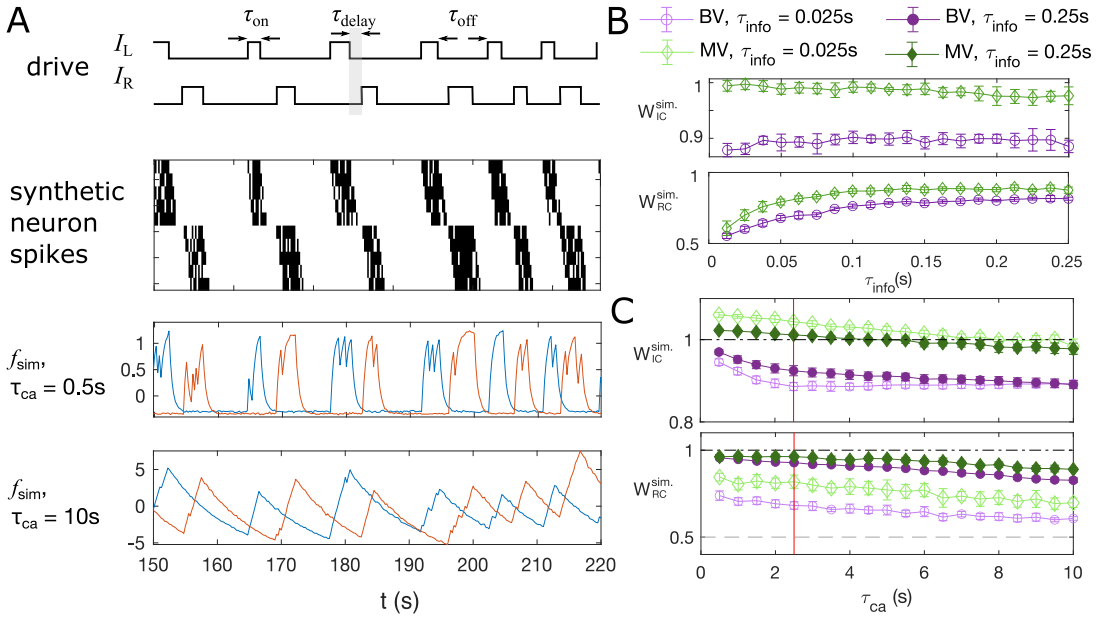

FIG. 5: **Synthetic data mimicking bursting motoneurons shows the slow timescale of calcium signal decay decreases GC performance.** (A) Example traces of the synthetic data for two chains of five neurons. The common stimuli, I_L and I_R, are sampled using the empirically observed on- and off-durations for the neuron bursts (τ_{on} and τ_{off}). The time delay of the onset of the right stimulus I_R from the offset of the left stimulus I_L is also sampled using empirical distribution. (B) Success of information flow retrieval, measured by the weight of the ipsilateral GC links, W_{IC}, and the weight of rostral-to-cordal links, W_{RC}, as a function of the information propagation time scale τ_{info}, evaluated at the empirical time scales $\tau_{ca} = 2.5$s, $\tau_{sampling} = 0.25$s, and biologically reasonable base spike rate $\lambda_0 = 32\text{s}^{-1}$. Results from bivariate GC are plotted in *purple*, and results from multivariate GC are in *green*. (C) Success of information flow retrieval for $\tau_{info} = 0.025$s and $\tau_{info} = 0.25$s for synthetic data with different calcium decay time constants. Greater calcium decay constants lead to worse information retrivals. The empirical calcium time scale $\tau_{ca} = 2.5$s is indicated by the red vertical line.

D. Pipeline summary and GC analysis of motoneuron data

Putting together all the observations of the previous sections, we developed an improved Granger causality analysis pipeline (Figure 7A) to overcome the limitations of naive GC for the investigation of directional information flow in neuron calcium data. These improvements consist of both pre-processing the calcium traces (see Section II C) and determining a custom threshold for the significance testing of the presence of a GC link, to avoid the many false positive links that the naive GC analysis finds (see Section II C 8). Pre-processing the data aims to remove undesirable effects of noisy fluorescence signals and of motion artifacts on the GC results. The first step consists of selecting only neurons displaying calcium traces that match their expectation (Section II C 5): calcium traces with a low signal-to-noise ratio or inconsistent behavior should be disregarded. This step is particularly important for MVGC analysis, in which the traces of all neurons are used to determine the presence of a link between any pair of neurons. Second, we correct the instantaneous change in fluorescence caused by motion artifacts (Section II C 4). In the final pre-processing step, the calcium signals are smoothed to remove remaining noise (Section II C 6), especially noise that is correlated across neurons and that leads to spurious links in the BVGC approach, and missing links in the MVGC analysis. In the BVGC analysis, correlation in the noise might be perceived as a link between two neurons. In the MVGC case, the correlation in the noise of the receiving neuron and in the noise of neurons on which the GC is conditioned can hide the actual influence of the signal of the driving neuron on the signal of the receiving neuron.

After these pre-processing steps, one can apply the GC algorithm to these calcium traces. In order to avoid calculating GC for many time lags, the choice of this parameter can be chosen to match biological delay of information flow – here 750 ms. For each pair of neurons, we time-shift one of the calcium traces in the GC analysis of a pair of neurons to remove causality between the two signals and use this new null model to determine the significance threshold, as motivated in Section II C 8. Notice that for some datasets, the resulting MVGC network has more connections than the corresponding BVGC network. This is because the adaptive thresholds for the significance test are chosen separately for BVGC and MVGC analysis.

We take advantage of anatomical knowledge of the expected network for the motoneuron data set to compare the naive GC results to our customized GC results. The improved GC pipeline significantly increases the W_{IC} ra-

bioRxiv preprint doi: https://doi.org/10.1101/2022.06.27.497721; this version posted June 29, 2022. The copyright holder for this preprint (which was not certified by peer review) is the author/funder. All rights reserved. No reuse allowed without permission.

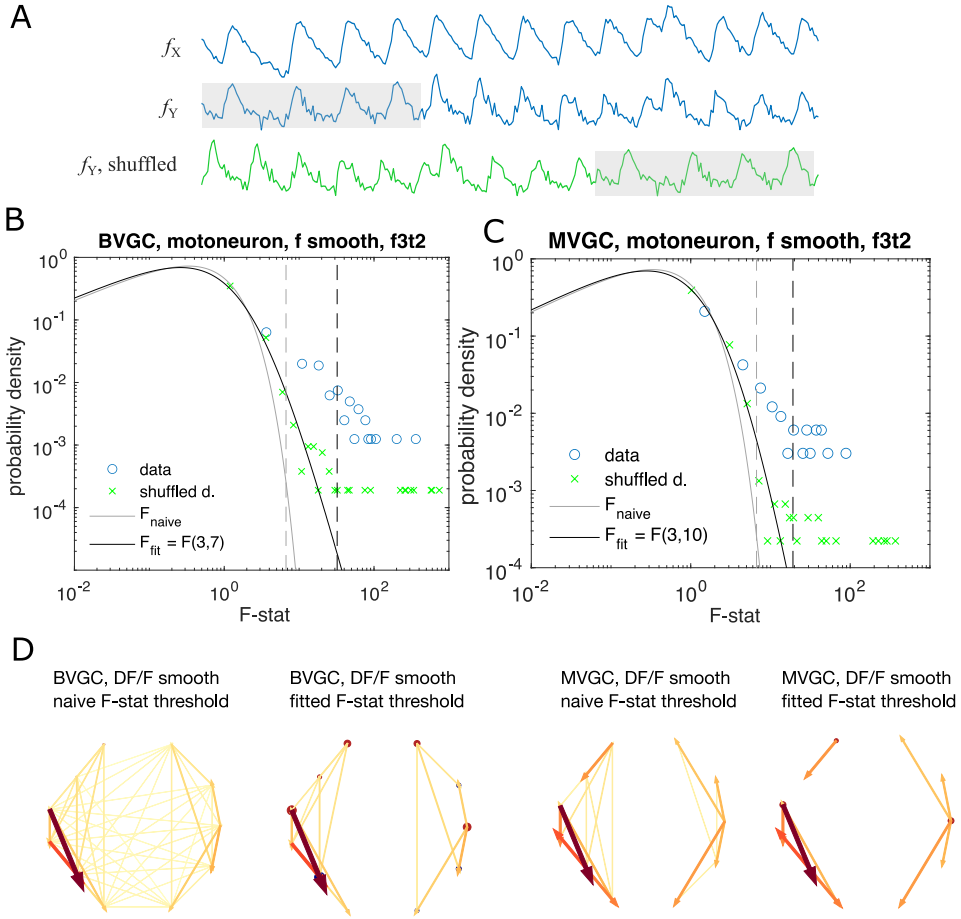

FIG. 6: **Significance tests for Granger causality on real calcium data require new thresholds, generated using null models.** (A) Schematics for generating null models by randomly shuffling the data. The *blue* dots and curves correspond to the original data, the effect neuron f_X and the cause neuron f_Y; the *green* ones are generated by random cyclic shuffling of the original $f_Y(t)$, with gray rectangles indicating matching time points before and after the cyclic shuffle. (B) The probability density of the F-statistics of the bivariate Granger causality for an example experiment (dataset *f3t2* from [32]). Blue circles are computed using the smoothed Calcium signals, and the green crosses are computed using the null model generated with cyclic shuffles. The black curve is the F-distribution used in the naive discrimination of GC statistics, and the gray curve is the best fitted F-distribution, fitting an effective number of samples. The gray and the black dashed vertical lines indicate the significance threshold for Granger causality, using the original threshold and the fitted threshold, respectively. (C) Same as (B), for multivariate Granger causality analysis. (D) Comparison between the significant GC network for the experiment *f3t2* using the naive vs. fitted F-statistics threshold.

tio from 0.62 ± 0.15 to 1.00 ± 0.00 for both BVGC and MVGC ($p < 0.001$). $W_{\mathrm{IC}} = 1$ indicates that there are no contralateral flow, corresponding to what is known from anatomy. On the other hand, the W_{RC} ratio does not significantly increase (0.59 ± 0.09 to 0.59 ± 0.15 for BVGC and 0.52 ± 0.08 to 0.53 ± 0.10 for MVGC, $p > 0.05$) (Figure 7B). W_{RC} close to 0.5 shows that GC analysis is unable to capture the rostrocaudal information flow pattern.

The improvement of the ipsilateral ratio can be explained by the disappearance of most contralateral links that were spuriously detected by the naive GC analysis. The rostrocaudal ratio W_{RC} is however not significantly improved. The temporal resolution of the recording (4 Hz leading to one frame every 250 ms) may not be sufficient to correctly determine the directionality of the information flow as is much slower than the actual propagation speed (a few ms, see [36]). In a similar manner, the decay time-constant of GCaMP3 is large compared to the refractory period between two spikes. Results could be further improved by recording at higher frequency and using novel fluorescent calcium sensors such as GCaMP6f, which has faster kinetics.

E. GC analysis for hindbrain data

In order to investigate the information flow between neurons in a more complex dataset, we analyzed population recordings from neurons in the hindbrain of larval zebrafish (data from [33], also see Figure 8AB). On each

bioRxiv preprint doi: https://doi.org/10.1101/2022.06.27.497721; this version posted June 29, 2022. The copyright holder for this preprint (which was not certified by peer review) is the author/funder. All rights reserved. No reuse allowed without permission.

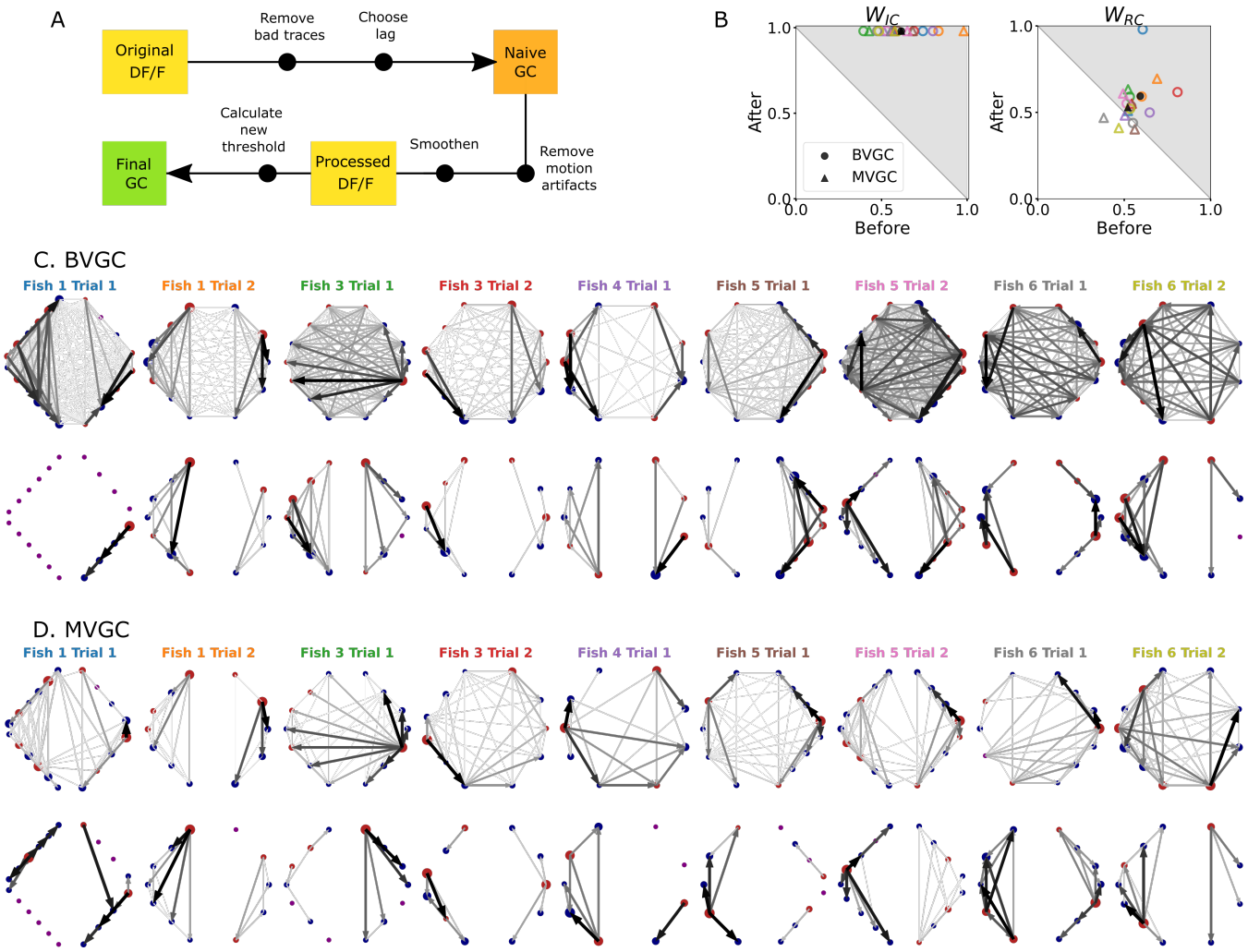

FIG. 7: **Comparison of GC analysis results with and without processing the calcium transients and adapting the threshold.** (A) Description of the whole pipeline. Before running the GC analysis on the raw calcium transients (DF/F), the lag parameter must be chosen. Then, before running the GC analysis again, motion artifacts are corrected, the fluorescence is smoothed and a new threshold is calculated. (B) Comparison of W_{IC} and W_{RC} before and after applying the pipeline to the GC analyses. Points in the upper right triangle gray-shaded area represent the ratios that have increased in the final GC results. Each fish is represented by a color, BVGC by circles and MVGC by triangles. Means are shown in black. We find that using our pipeline, W_{IC} strongly increases and we can clear out the spurious contra-lateral links present in the original GC. W_{RC} is not significantly improved: the recording frequency and GCaMP decay are likely too low and slow compared to the speed of rostro-caudal propagation of the information flow. (C) Network results before and after applying our pipeline, for all fish. For consistency in the network representation and better ability to compare, we removed the uncharacteristicly behaving neurons of the GC analysis before applying the pipeline. Note that more links are found on the side that was better in focus in the recording.

plane, up to 150 neurons were recorded *in vivo* using two-photon calcium imaging at 5.81 Hz across the whole hindbrain of *Tg(HUC:GCaMP5G)* transgenic larval zebrafish performing the optomotor response ($n = 139$ neurons in Fig 8A). Because V2a neurons localised in the medial hindbrain are well-known command neurons driving locomotion [42, 43], we focused our analyses on medial neurons whose activity was correlated to swimming (red neurons in the rectangle, $n_{\mathrm{med}} = 20$, in Fig 8A, B). The corresponding calcium traces (Fig 8B) were exempt of motion artifacts. We did not smooth as the scanning of the two-photon microscope led to noise that is not correlated between neurons. None of the pre-processing described above was therefore necessary for this dataset.

When applying the naive bivariate Granger causality using the original threshold, we found all links to be significant (Fig 8C), suggesting numerous spurious links due to the high overall correlation in neuron activity. We found that motor-correlated neurons exhibited a higher drive (Fig 8D), defined as the sum of all its outgoing GC

bioRxiv preprint doi: https://doi.org/10.1101/2022.06.27.497721; this version posted June 29, 2022. The copyright holder for this preprint (which was not certified by peer review) is the author/funder. All rights reserved. No reuse allowed without permission.

links:

$$\text{drive}_i = \sum_j GC_{i\to j} \tag{14}$$

where j spans all other neurons.

The drive was not correlated to the neuron's position along the scanning direction (correlation of $r = 0.15$ across all 139 neurons and $r = 0.03$ across medial swim-correlated neurons, $p > 0.05$, Fig S8A), implying that a correction for the scanning delay of the two-photon microscope was not necessary. However, the drive for a given neuron was correlated to the signal-to-noise ratio (SNR) of the calcium transient, computed following details in **Materials and Methods**, with a Pearson's correlation coefficient of $r = 0.45$ across all neurons and $r = 0.69$ across medial neurons, $p < 0.001$, Fig 8D. This effect can be corrected using an adaptive threshold tailored to each neuron pair to normalize the GC values. We notice that the drive is higher in swim-correlated neurons, especially in medial neurons, further justifying focusing our attention on this subset of neurons.

To remove the spurious connections, we computed, as introduced before, the custom threshold for the significance testing of GC links. The difference from motoneuron data is that the hindbrain activities are driven by a periodic stimulus. Therefore, to generate the null statistics, we randomize the neural activities of the driver neurons by shuffling the neural signals, while keeping the stimulus fixed. More specifically, we divide the entire recording into 19 epochs of consecutive onset (10 seconds) and offset (5 seconds) of the stimulus (see Fig. 8B), and generate shuffled calcium traces by randomizing the order of these 19 epochs.

For each neuron pair (i, j), we apply m such random shuffles to the calcium trace of the driver neuron i, and compute the F-statistics $\{F^{\text{shuffled}}_{i\to j}\} = \{F^{s_1}_{i\to j}, \ldots, F^{s_m}_{i\to j}\}$. For BVGC, $m = 1000$, and for MVGC, $m = 100$. We denote the empirical distribution of $\{F^{\text{shuffled}}_{i\to j}\}$ by $\mathcal{F}^{\text{shuffled}}$. As in the previous examples, we need to parameterize $\mathcal{F}^{\text{shuffled}}_{i\to j}$. As before, we noticed that for each neuron pair (i, j), the distribution $\mathcal{F}^{\text{shuffled}}_{i\to j}$ is well-described by a constant-rescaled F-distribution (Fig S9). Applying an adaptive threshold on $F_{i\to j}$ reduces to applying the original threshold on the normalized $\widetilde{F}_{i\to j}$, defined by dividing the naive F-statistics with the expectation value of the F-statistics generated by the shuffled data. Mathematically,

$$\widetilde{F}_{i\to j} = F_{i\to j}/\langle F^{\text{shuffled}}_{i\to j}\rangle. \tag{15}$$

Finally, by analogy, we use Eq. 5 to compute the normalized version of the GC values, directly from the normalized F-statistics. The final BVGC matrix is shown in Fig 8E. Normalizing the BVGC values allowed the reduction of the correlation between the drive and the SNR, from 0.69 to now 0.49 for medial motor-correlated neurons (Fig 8F).

With this new threshold for significance, most spurious links disappeared. The remaining significant BVGC links between medial motor-correlated neurons were rostral-to-caudal and caudal-to-rostral, as well as ipsilateral and contralateral, showing strong information flow between these key command neurons. The MVGC resulted in a much small number of significant links (Fig 8G), suggesting a strong global correlation between the neurons.

III. DISCUSSION

Granger causality is a simple and effective method for information flow retrieval in large brain areas [27–29]. However, to apply GC analysis on calcium signals from population of neurons at single-cell level requires a careful re-examination of the method, because of the nonlinearity, non-Gaussianity, and the predominance of correlated noise in the data. We have developed an improved analysis pipeline and demonstrated its usefulness in retrieving information flow in motoneurons [32] and hindbrain neurons [34] in zebrafish. Since the properties of calcium signals in neuronal populations are comparable across animal models, the tailored analysis pipeline we are proposing is not limited to zebrafish, and can be applied to calcium imaging data across animal species.

The first concern of applying GC analysis to calcium signals is how well GC, a measure of linear dependence among signals, can retrieve information flow in this nonlinear and non-Gaussian imaging data. Using synthetic data on small networks with different types of dynamics, ranging from linear autoregressive models to spiking dynamics with exponential decay, designed to mimick calcium signals, we have demonstrated that GC can successfully reconstruct the underlying true dynamical interactions among neurons for a wide range of dynamical variables. For motoneurons that fire repeatedly in bursts, we modeled network activity with two chains of neurons using empirically identified dynamical parameters. By doing so, we showed that GC can retrieve the correct rostral-to-caudal information flow, even when the information propagation occurs at a faster scale than the experimental sampling time and the time decay of the calcium transient. Altogether our results on simulations show that GC remains a useful analysis method for population recordings of single-cell level calcium signals.

With improved confidence on the GC method, we apply GC to real calcium signals. Because real data is noisy, GC analysis on real calcium signals requires careful examination of multiple pitfalls that we addressed in our analysis pipeline.

1. *Preprocessing of calcium imaging data.* As reported previously [23, 24], we find that GC analysis is sensitive to correlated noise, which can often occur in calcium signals, due to, for example, motion artifacts or noise on the sensor. We highlighted that a motion artifact occurring at a single time point

bioRxiv preprint doi: https://doi.org/10.1101/2022.06.27.497721; this version posted June 29, 2022. The copyright holder for this preprint (which was not certified by peer review) is the author/funder. All rights reserved. No reuse allowed without permission.

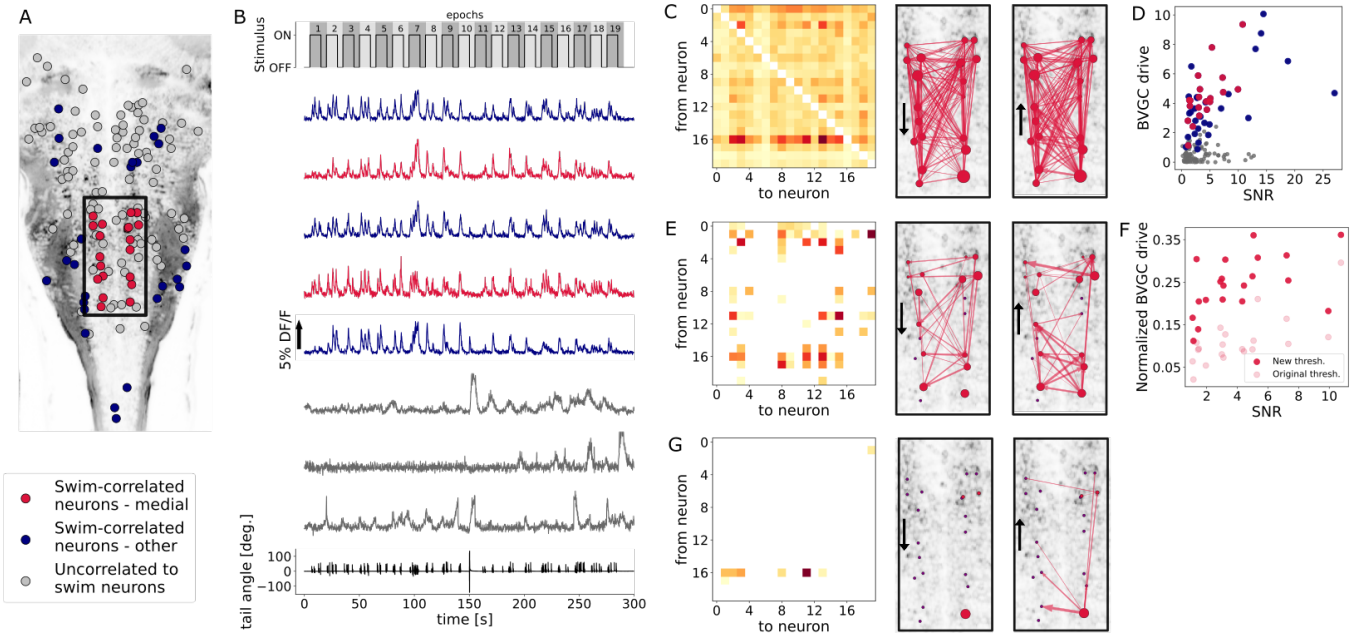

FIG. 8: **Application of the GC pipeline on neuronal populations recorded in the hindbrain of larval zebrafish performing the optomotor response.** (A) The population calcium imaging data was acquired *in vivo* using a laser scanning two-photon calcium imaging at 5.81 Hz at single-cell resolution of the hindbrain of *Tg(HUC:GCaMP5G)* transgenic larvae during active visuomotor behavior (data from [33]). Neurons ($n = 139$) in a given plane of the larval zebrafish hindbrain selected for analysis. The activity of neurons depicted in colors was correlated to motor: the red neurons located in the medial rectangle are in the location of the V2a stripe ($n = 20$), and all other motor-correlated neurons are depicted in blue ($n = 27$). The activity of neurons depicted in gray ($n = 112$) are not correlated to the motor output. (B) Example of calcium traces for the motor-correlated medial neurons (*red*), other motor-correlated neurons (*blue*) and non-motor correlated neurons (*gray*), ordered from top to bottom by their decreasing signal-to-noise ratio (SNR). The optomotor stimulus is depicted on top while the tail angle illustrating the motor output is depicted at the bottom. (C) GC matrix and map of information flow for the naive BVGC on medial motor-correlated neurons. All 380 possible pairs are found to have a significant drive. This fully-connected network suggests that the naive BVGC algorithm is too permissive to false positive links, and an adapted pipeline is needed to clean out the many spurious connections. (D) The neuronal drive, calculated as the sum of the strength of all outgoing GC links for each neuron, is correlated to the SNR of the calcium traces. It is especially high for medial neurons ($r = 0.69$, compared to $r = 0.45$ across all 139 neurons). (E) After we customized the threshold and normalized the GC values, we obtain a network with fewer remaining significant GC links, succeeding in removing many (spurious) links. We notice that the information flow was not unidirectional: links are rostral-to-caudal and caudal-to-rostral, as well as ipsilateral and contralateral, showing strong information flow between the medial motor-correlated neurons. (F) When computing the drive on the GC normalized by the new threshold, the correlation with the SNR decreases from 0.69 to 0.49 for medial neurons. (G) The pipeline applied to MVGC removes too many links due to the high correlation in the data (all neurons are motor-correlated) and relatively high number of neurons (20).

can create spurious GC links and should therefore be removed before proceeding to GC analysis. Similarly, correlated noise across neurons throughout the measurement will also results in spurious links, and will be especially problematic for multivariate GC analysis. The pitfalls associated with correlated noise can be resolved by identifying statistical features of the noise during the decay of calcium signals, and subsequently removing them using total-variational regularization as we used here, or other nonlinear filtering methods.

2. *Adaptive threshold for significance test in GC analysis.* The naive GC analysis uses a significance test that compares the F-statistics with the null test, an F-distribution. While this null model is exact for Gaussian processes, for real data with nonlinear dynamics, non-Gaussian noise or data with periodic stimuli, the null distribution often deviates and needs to be learned through randomization of the data. In order to develop a more stringent test of significance for GC links, we generated null models of the F-statistics using random cyclic shuffles of the real data. By using a pair-specific threshold for the F-statistics, we were able to correct for the effect of the signal-to-noise ratio on the GC value.

Applied to motoneuron data, the new pipeline led to an improvement in identifying the directionality of ispilateral, but in not the rostro-caudal GC links likely due to the small temporal resolution of the data.

For population recordings of hindbrain neurons, our

bioRxiv preprint doi: https://doi.org/10.1101/2022.06.27.497721; this version posted June 29, 2022. The copyright holder for this preprint (which was not certified by peer review) is the author/funder. All rights reserved. No reuse allowed without permission.

new pipeline revealed that compared to neurons whose activity did not encode the motor output, motor-related neurons, located in the area of the V2a stripe [44] in particular, were more likely to drive the activity of other neurons. When calcium traces were acquired with a spinning disk microscope, i.e. using a camera chip for detection, the noise was correlated because all the pixels over the field of view were recorded at the same time. In this case, smoothing the fluorescence traces was consequently necessary. In contrast, this step is not crucial with two-photon laser scanning microscopes and light-sheet microscopes in which different pixels and planes respectively were scanned across the sample.

In the acquisition conditions we used, with >5Hz per plane using two-photon laser scanning microscopy, we found that the scanning direction, which results in a small delay between the time at which pixels were acquired, did not influence the GC results. Neurons recorded at the beginning of the scanning cycle did not appear as driver neurons of neurons recorded at the end of the cycle. We found however that the drive of a given neuron correlated with the signal-to-noise ratio (SNR) of the calcium trace. We found after computing the new threshold for significance with a corrected null hypothesis and the normalized GC values that the correlation between the drive and SNR decreased.

We have focused in this manuscript on issues specific to calcium imaging. Here, we briefly discuss problems that are also common to other neural data types such as fMRI. Firstly, we emphasize that with current experimental techniques, only a small portion of the entire nervous systems is recorded. GC does not allow identification of the true underlying connection in the presence of unobserved neurons, nonetheless, it is able to identify information flow and an effective functional causal network for the observed neurons. Another issue specific to multivariate GC is the problem of overfitting [15], especially when the number of neurons is large compare to the number of independent samples in the data. In this situation, one would need to consider group the activities of neurons [45], either according to their correlation, or by adjacency, and apply GC to this coarse-grained network. One can also apply GC to subnetworks of observed neurons, and construct a distribution of information flows.

Other approaches to identifying causal links than GC have been developed and applied in genomic data [46], gene regulatory networks [47] and large scale neural networks [48]. Further work is needed to explore whether and how these approaches could be adapted to calcium recordings.

Comparing to common practices of using correlation to extract a functional network from calcium neural signals, our GC pipeline provides more information such as the direction of information flow. Additionally, compared to existing methods to target the pitfalls of calcium data, such as addressing the global additive noise using a inverse-time GC [24], our pipeline preprocesses the calcium signal taking advantage of its slow decay, and keeps the GC approach as a simple method. By writing down GC value as a function of the F-statistics, normalized by null models directly constructed using shuffled data, we are able to correct the GC network by adjusting the value of individual links, and to reduce the influence of signal-to-noise ratio in a simple yet effective way. With the improved pipeline, we are now ready to apply Granger causality analysis to data from experiments that simultaneously record from high numbers of neurons in larger networks.

IV. MATERIALS AND METHODS

A. Synthetic dynamics on small networks

We simulate artificial neural networks with three different dynamics, evolving at a time resolution of Δ_{sim}. For simplicity, we set the information flow to occur at the same time delay.The memory kernel, or the influence of neuron j on neuron i separated by time lag of q (in the unit of Δ_{sim}), is denoted as $\Gamma_{ij,q}$. The three methods are:

1. *Vector autoregression models* (VAR)

$$f_{i,t} = \sum_{q=1}^{L_{\text{true}}} \sum_{j} \Gamma_{ij,q} f_{j,t-q} + \xi_{i,t},$$

where $\xi_{i,t}$ is a white noise. The vector autoregression model is identical to the underlying model for Granger causality analysis, and allow GC to best reproduce the network structure.

2. *Spike dynamics for generalized linear model* (GLM) A simple method to simulate spiking neurons with non-linear interaction is through the generalized linear model (GLM), where the spiking rates of the neurons are given by

$$\lambda_{i,t} = \exp\left(\mu_i + \sum_{q=1}^{L_{\text{true}}} \sum_{j} \Gamma_{ij,q} \sigma_{j,t-q}\right)$$

and the spike counts

$$\sigma_{i,t} \sim \text{Poiss}(\lambda_{i,t}).$$

Here, μ_i gives a base rate for spiking, $\Gamma_{ij,q}$ is how the spike rates depend on the neurons' past history. The spike counts $\sigma_{i,t}$ are what we consider as synthetic data, and what we will use for Granger causality analysis.

3. *Spike dynamics regressed by exponential decay* (GLM-Calcium) To simulate Calcium neuronal data, which has a fast onset and a slow decay, we add an exponential regression to the spike simulation with the GLM. The resulting trace is

$$f_{i,t} = \sum_{q=0}^{\infty} \sigma_{i,t-q} e^{-q/\tau_{\text{ca}}} \Delta_{\text{sim}}$$

bioRxiv preprint doi: https://doi.org/10.1101/2022.06.27.497721; this version posted June 29, 2022. The copyright holder for this preprint (which was not certified by peer review) is the author/funder. All rights reserved. No reuse allowed without permission.

We simulate the above three dynamics with identical interaction network $\Gamma_{ij,q}$. The network has equal numbers of excitatory and inhibitory neurons to ensure that the dynamics is stationary. For convenience, the strength of the connection is set to be identical, $\Gamma_{ij,q}|_{q<L_{\text{true}}} = cA_{ij}$, where c is the connection strength, and A_{ij} is the signed adjacency matrix.

B. Cross-correlation

The simplest approach of finding links in networks is through cross-correlation,

$$C_{ij}(\Delta t) = \frac{\sum_t (f_i(t) - \overline{f_i})(f_j(t+\Delta t) - \overline{f_j})}{\sigma_{f_i}\sigma_{f_j}}. \tag{16}$$

The (equal-time) correlation matrix given by $C_{ij}(\Delta t = 0)$ is commonly used in calcium signal analysis as a functional network. Nonetheless, it is symmetric, and does not reveal directional information.

C. Smooth calcium trace using total variation regularization

We follow the same procedure as in [39] to smooth calcium traces using total variation regularization. Existing MATLAB packages and custom code are used to reconstruct the smooth trace [40]. Here, we outline this smoothing method briefly.

Consider a raw calcium fluorescence signal $f(t)$ from neurons that are known to generate episodic spikes and silences. These episodic activities can be characterized by the underlying derivative signal $u(t)$ which governs the onset and offset of the episodes, which we assume have an exponentially distributed temporal variations, and is only weakly correlated in time. If we further assume that the noise in f is Gaussian and white, the maximum likelihood reconstruction of the signal $f(t)$ is equivalent to minimizing

$$F(u) = \frac{\tau_f}{\sigma_f}\int_0^T dt|\dot{u}| + \frac{1}{2\sigma_n^2\tau_n}\int_0^T dt|Au - f|^2\,, \tag{17}$$

where A is the antiderivative operator, the combination $\sigma_n^2\tau_n$ is the spectral density of noise floor that we can retrieve from the power spectrum of f at high frequencies, σ_f is the total standard deviation of the signal, and τ_f is the typical time scale of these variations. We determine the one unknown parameter τ_f by asking that, after smoothing, the cumulative power spectrum of the residue $Au - f$ has the least root mean square difference from the cumulative power spectrum of the extrapolated white noise.

D. Compute signal-to-noise ratio

We compute the signal-to-noise ratio (SNR) for the fluorescence trace of a neuron, $f(t)$, using the smoothing procedure in the previous section (Sec. IV C). Namely, for each trace $f(t)$, we first apply the smoothing procedure. Then, the power of the noise, P_{noise}, is given by the extrapolated white noise, and equivalently by the sum of the power spectrum of the residue $Au - f$. The sum of the power spectrum of f gives the sum of the power of the noise and the power of the signal, $P_{\text{signal}} + P_{\text{noise}}$. Finally, the SNR is computed as the ratio of $P_{\text{signal}}/P_{\text{noise}}$.

E. Synthetic statistical data generation

To study the effect of slow calcium decays on the accuracy of GC analysis, we generate synthetic data statistically. Specifically, we consider two chains of five neurons, driven externally by blocked stimulus with progressing time-delay across each chain, and alternates between the left and the right side. The stimulus of the left-side is generated by choosing intervals, τ_{on}, for consecutive on-state (and τ_{off} for consecutive off-states) uniformly from the set $\left[\min(\tau_{\text{on}}^{\text{data}}), \max(\tau_{\text{on}}^{\text{data}})\right]$, where the $\{\tau_{\text{on}}^{\text{data}}\}$ is the set of duration of all "on"-states in a real zebrafish experiment, founded by positive finite difference in the fluorescent signal smoothened by total-variational regularization. The stimulus of the right-side follows with the delay time τ_{delay} also matches the uniform distribution on the support of the empirical distribution.

We model the sequential activation of the motoneurons by imposing the spike rate as

$$\lambda_{\text{L}_k}(t) = I_{\text{L}}(t - k\tau_{\text{info}})\lambda_0,$$
$$\lambda_{\text{R}_k}(t) = I_{\text{R}}(t - k\tau_{\text{info}})\lambda_0,$$

where k is the ordered index of neurons on each side, τ_{info} is the time scale of information propagation, and λ_0 is a large basal spike rate to simulate the plateau in the neural activity. We use a standard Poisson process with these rates to generate the spike train for each neuron, $\{\sigma_i, t\}$. Finally, the observed calcium signal is computed by convoluting the spikes with exponential decays for each neuron i,

$$f_{i,t} = \sum_{q=0}^{\infty} \sigma_{i,t-q} e^{-q/\tau_{\text{ca}}} \Delta_{\text{sim}}$$

and downsampling at a sampling frequency $\tau_{\text{sampling}}^{-1}$.

Data availability

All data used in our manuscript have been previously published [32, 33]. The MATLAB code

bioRxiv preprint doi: https://doi.org/10.1101/2022.06.27.497721; this version posted June 29, 2022. The copyright holder for this preprint (which was not certified by peer review) is the author/funder. All rights reserved. No reuse allowed without permission.

to generate synthetic data, and the python pipeline for the improved GC analysis can be found in https://github.com/statbiophys/zebrafishGC.git.

Acknowledgement

We thank Urs Böhm and Kristen Severi for providing feedback on the data from Severi et al 2019 and Fabrizio De Vico Fallani, Mario Chavez (Paris Brain Institute) and Moritz Grosse-Wentrup (University of Wien) for insightful feedback. This work was supported by the European Research Council Consolidator Grants n. 724208 (AMW) and n. 101002870 (CW), the New York Stem Cell Foundation (NYSCF) Robertson Award 2016 #NYSCF-R-NI39 (CW), the Human Frontier Science Program (HFSP) Research Grant #RGP0063/2018 (CW), the Fondation pour la Recherche Médicale Team grant (FRM- EQU202003010612) and the Fondation Bettencourt-Schueller #FBS-don-0031 (CW).

[1] Deisseroth K (2011) Optogenetics. Nature methods 8:26–29.
[2] Fenno L, Yizhar O, Deisseroth K (2011) The development and application of optogenetics. Annual review of neuroscience 34:389–412.
[3] Ahrens MB, Orger MB, Robson DN, Li JM, Keller PJ (2013) Whole-brain functional imaging at cellular resolution using light-sheet microscopy. Nature methods 10:413–420.
[4] Nguyen JP, et al. (2016) Whole-brain calcium imaging with cellular resolution in freely behaving caenorhabditis elegans. Proceedings of the National Academy of Sciences 113:E1074–E1081.
[5] Venkatachalam V, et al. (2016) Pan-neuronal imaging in roaming caenorhabditis elegans. Proceedings of the National Academy of Sciences 113:E1082–E1088.
[6] Cong L, et al. (2017) Rapid whole brain imaging of neural activity in freely behaving larval zebrafish (*danio rerio*). Elife 6.
[7] Goulding M (2009) Circuits controlling vertebrate locomotion: moving in a new direction. Nature Reviews Neuroscience 10:507–518.
[8] Bastos AM, Schoffelen JM (2016) A tutorial review of functional connectivity analysis methods and their interpretational pitfalls. Frontiers in systems neuroscience 9:175.
[9] Cohen MR, Kohn A (2011) Measuring and interpreting neuronal correlations. Nature neuroscience 14:811–819.
[10] Haesemeyer M, Robson DN, Li JM, Schier AF, Engert F (2018) A brain-wide circuit model of heat-evoked swimming behavior in larval zebrafish. Neuron 98:817–831.
[11] Stringer C, et al. (2019) Spontaneous behaviors drive multidimensional, brainwide activity. Science 364:eaav7893.
[12] Granger CW (1969) Investigating causal relations by econometric models and cross-spectral methods. Econometrica: journal of the Econometric Society pp 424–438.
[13] Geweke J (1982) Measurement of linear dependence and feedback between multiple time series. Journal of the American statistical association 77:304–313.
[14] Geweke JF (1984) Measures of conditional linear dependence and feedback between time series. Journal of the American Statistical Association 79:907–915.
[15] Seth AK, Barrett AB, Barnett L (2015) Granger causality analysis in neuroscience and neuroimaging. Journal of Neuroscience 35:3293–3297.
[16] Gow Jr DW, Segawa JA, Ahlfors SP, Lin FH (2008) Lexical influences on speech perception: a granger causality analysis of meg and eeg source estimates. Neuroimage 43:614–623.
[17] Roebroeck A, Formiethano E, Goebel R (2005) Mapping directed influence over the brain using granger causality and fmri. Neuroimage 25:230–242.
[18] Deshpande G, LaConte S, James GA, Peltier S, Hu X (2009) Multivariate granger causality analysis of fmri data. Human brain mapping 30:1361–1373.
[19] Wen X, Rangarajan G, Ding M (2013) Is granger causality a viable technique for analyzing fmri data? PloS one 8:e67428.
[20] Brovelli A, et al. (2004) Beta oscillations in a large-scale sensorimotor cortical network: directional influences revealed by granger causality. Proceedings of the National Academy of Sciences 101:9849–9854.
[21] Florin E, Gross J, Pfeifer J, Fink GR, Timmermann L (2010) The effect of filtering on granger causality based multivariate causality measures. Neuroimage 50:577–588.
[22] Stokes PA, Purdon PL (2017) A study of problems encountered in granger causality analysis from a neuroscience perspective. Proceedings of the national academy of sciences 114:E7063–E7072.
[23] Nalatore H, Ding M, Rangarajan G (2007) Mitigating the effects of measurement noise on granger causality. Physical Review E 75:031123.
[24] Vinck M, et al. (2015) How to detect the granger-causal flow direction in the presence of additive noise? Neuroimage 108:301–318.
[25] Zhou D, Zhang Y, Xiao Y, Cai D (2014) Analysis of sampling artifacts on the granger causality analysis for topology extraction of neuronal dynamics. Frontiers in computational neuroscience 8:75.
[26] Barnett L, Seth AK (2017) Detectability of granger causality for subsampled continuous-time neurophysiological processes. Journal of neuroscience methods 275:93–121.
[27] Shojaie A, Fox EB (2021) Granger causality: A review and recent advances. Annual Review of Statistics and Its Application 9.
[28] Barnett L, Barrett AB, Seth AK (2018) Solved problems for granger causality in neuroscience: A response to stokes and purdon. NeuroImage 178:744–748.
[29] Nicolaou N, Hourris S, Alexandrou P, Georgiou J (2012) Eeg-based automatic classification of 'awake'versus 'anesthetized'state in general anesthesia using granger causality. PloS one 7:e33869.
[30] Kim S, Putrino D, Ghosh S, Brown EN (2011) A granger

bioRxiv preprint doi: https://doi.org/10.1101/2022.06.27.497721; this version posted June 29, 2022. The copyright holder for this preprint (which was not certified by peer review) is the author/funder. All rights reserved. No reuse allowed without permission.

causality measure for point process models of ensemble neural spiking activity. PLoS computational biology 7:e1001110.

[31] Gerhard F, et al. (2013) Successful reconstruction of a physiological circuit with known connectivity from spiking activity alone. PLoS computational biology 9:e1003138.

[32] De Vico Fallani F, Corazzol M, Sternberg JR, Wyart C, Chavez M (2014) Hierarchy of neural organization in the embryonic spinal cord: Granger-causality graph analysis of in vivo calcium imaging data. IEEE Transactions on Neural Systems and Rehabilitation Engineering 23:333–341.

[33] Severi KE, Böhm UL, Wyart C (2018) Investigation of hindbrain activity during active locomotion reveals inhibitory neurons involved in sensorimotor processing. Scientific reports 8:1–11.

[34] Oldfield CS, et al. (2020) Experience, circuit dynamics, and forebrain recruitment in larval zebrafish prey capture. Elife 9:e56619.

[35] Buss R, Drapeau P (2001) Synaptic drive to motoneurons during fictive swimming in the developing zebrafish. Journal of Neurophysiology 86:197–200.

[36] Masino M, Fetcho J (2005) Fictive swimming motor patterns in wild type and mutant larval zebrafish. Journal of neurophysiology 93:3177–3188.

[37] Warp E, et al. (2012) Emergence of patterned activity in the developing zebrafish spinal cord. Current Biology 22:93–102.

[38] Saint-Amant L, Drapeau P (2001) Synchronization of an embryonic network of identified spinal interneurons solely by electrical coupling. Neuron 31:1035–1046.

[39] Chen X, Randi F, Leifer AM, Bialek W (2019) Searching for collective behavior in a small brain. Physical Review E 99:052418.

[40] Chartrand R (2011) Numerical differentiation of noisy, nonsmooth data. ISRN Appl. Math. 2011.

[41] Tian L, Hires SA, Looger LL (2012) Imaging neuronal activity with genetically encoded calcium indicators. Cold Spring Harbor Protocols 2012:pdb–top069609.

[42] Kimura Y, et al. (2013) Hindbrain v2a neurons in the excitation of spinal locomotor circuits during zebrafish swimming. Current Biology 23:843–849.

[43] Pujala A, Koyama M (2019) Chronology-based architecture of descending circuits that underlie the development of locomotor repertoire after birth. Elife 8:e42135.

[44] Kinkhabwala A, et al. (2011) A structural and functional ground plan for neurons in the hindbrain of zebrafish. Proceedings of the National Academy of Sciences 108:1164–1169.

[45] Meshulam L, Gauthier JL, Brody CD, Tank DW, Bialek W (2019) Coarse graining, fixed points, and scaling in a large population of neurons. Physical review letters 123:178103.

[46] Verny L, Sella N, Affeldt S, Singh PP, Isambert H (2017) Learning causal networks with latent variables from multivariate information in genomic data. PLoS computational biology 13:e1005662.

[47] Meinshausen N, et al. (2016) Methods for causal inference from gene perturbation experiments and validation. Proceedings of the National Academy of Sciences 113:7361–7368.

[48] Ke NR, et al. (2019) Learning neural causal models from unknown interventions. arXiv preprint arXiv:1910.01075.

[49] Barnett L, Seth AK (2014) The mvgc multivariate granger causality toolbox: a new approach to granger-causal inference. Journal of neuroscience methods 223:50–68.

Supplementary information

bioRxiv preprint doi: https://doi.org/10.1101/2022.06.27.497721; this version posted June 29, 2022. The copyright holder for this preprint (which was not certified by peer review) is the author/funder. All rights reserved. No reuse allowed without permission.

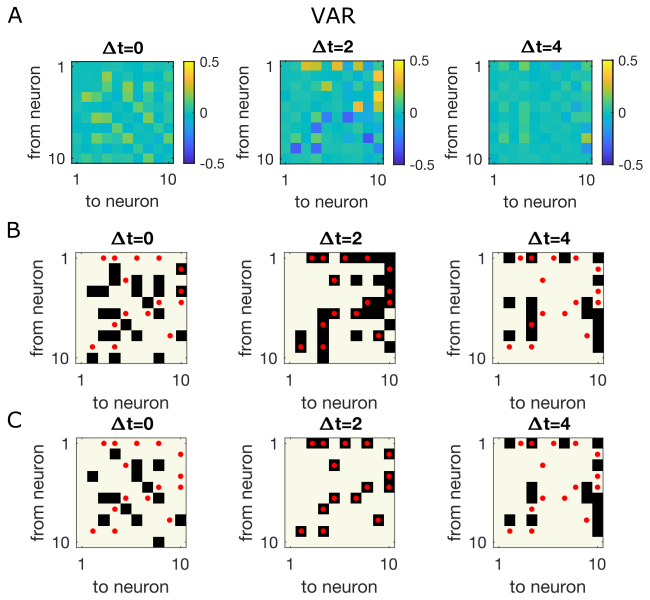

FIG. S1: Cross-correlation of the signal does not return the underlying interaction network: simulate VAR dynamics. (A) Cross-correlation matrix at $\Delta t = 0, 2, 4$. The true underlying dynamics has neuron-neuron interaction for $\Delta t = 1, 2$. (B) Significant cross-correlations are marked by black squares, while the true underlying network is indicated by red dots. (C). Links with top absolute value of cross-correlations, with the number of total links matching that of the true underlying connectivity.

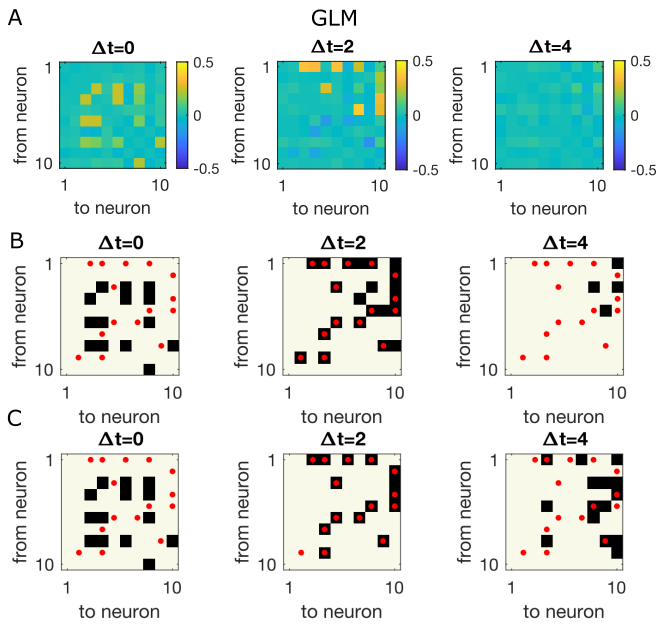

FIG. S2: Same as Fig. S1, for synthetic data generated using GLM dynamics.

bioRxiv preprint doi: https://doi.org/10.1101/2022.06.27.497721; this version posted June 29, 2022. The copyright holder for this preprint (which was not certified by peer review) is the author/funder. All rights reserved. No reuse allowed without permission.

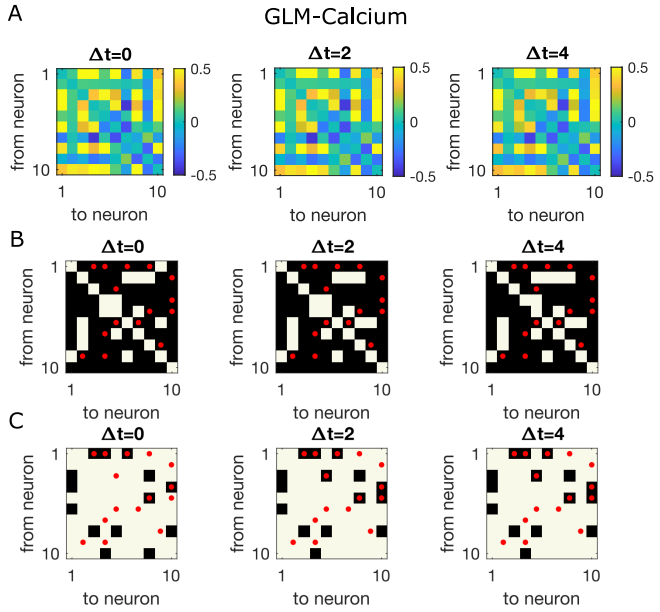

FIG. S3: Same as Fig. S1, for synthetic data generated using GLM-calcium dynamics.

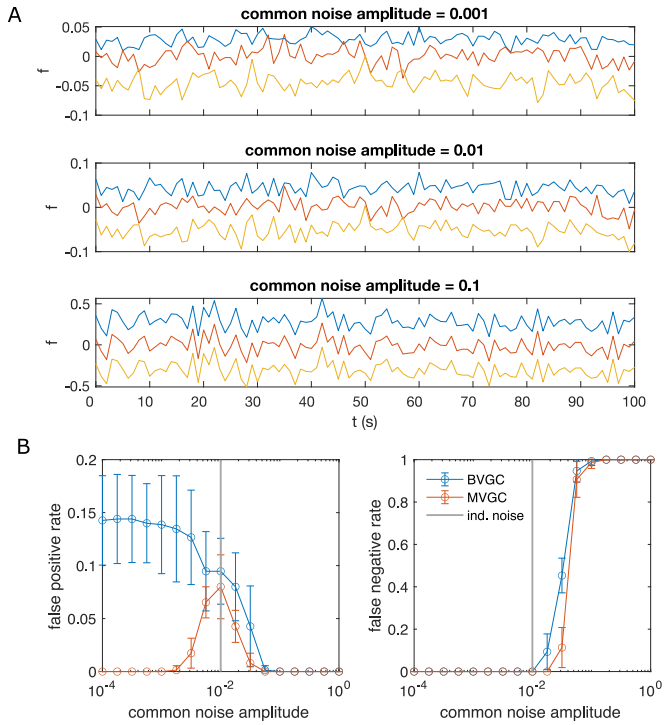

FIG. S4: Correlated noise increases the error of Granger causality analysis, exemplified by synthetic data generated by VAR dynamics and corrupted by a system-wide shared noise. (A) Example traces for VAR dynamics added with shared noise with increasing strength. (B) The error of GC analysis increases as the amplitude of the shared noise increases.

bioRxiv preprint doi: https://doi.org/10.1101/2022.06.27.497721; this version posted June 29, 2022. The copyright holder for this preprint (which was not certified by peer review) is the author/funder. All rights reserved. No reuse allowed without permission.

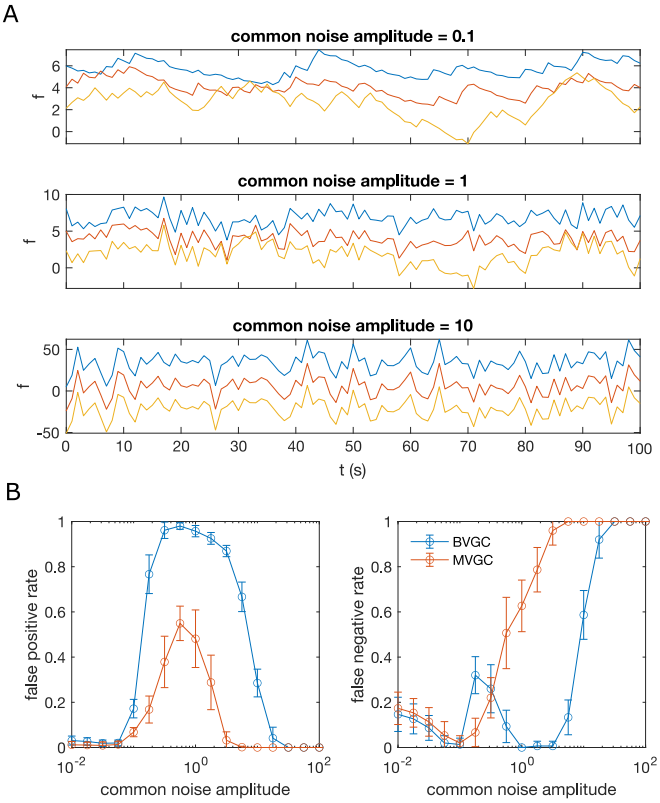

FIG. S5: Same as Fig. S4, but for data generated with GLM-calcium dynamics.

bioRxiv preprint doi: https://doi.org/10.1101/2022.06.27.497721; this version posted June 29, 2022. The copyright holder for this preprint (which was not certified by peer review) is the author/funder. All rights reserved. No reuse allowed without permission.

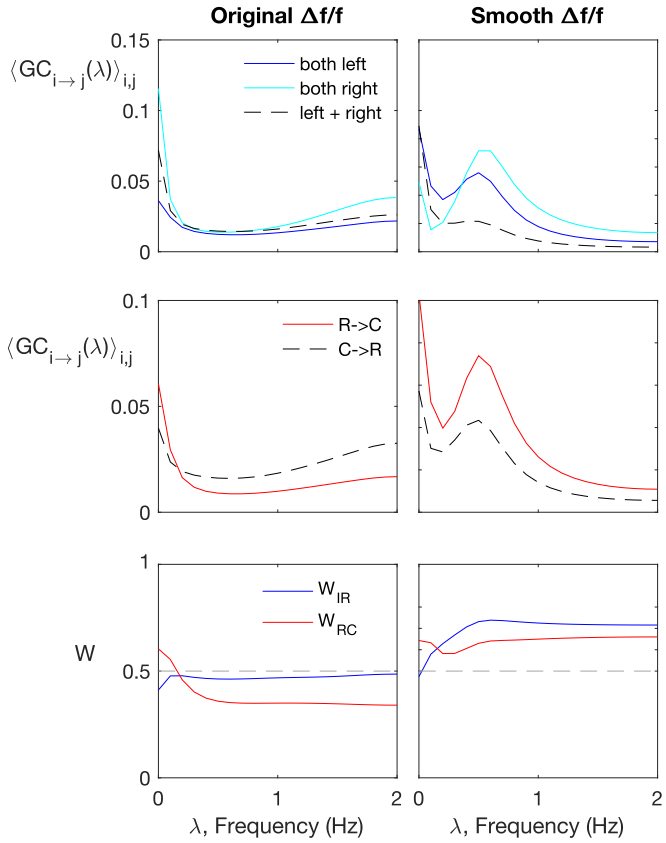

FIG. S6: Spectral Granger-causality (computed using the MATLAB package [49]). Results for motoneurons (dataset *f6t1*) reveals more structre when applied to smoothened fluorescence data compared to the raw fluorescence signal. The top row shows the ipsilatarel links in solid curves, and contralateral links in dashes. The top row shows the rostral-to-caudal links in solid curves, and caudal-to-rostral links in dashes. The last row shows the weighted ipsilateral ratio W_{ipsi} and the weighted rostral-to-caudal ratio W_{RC}.

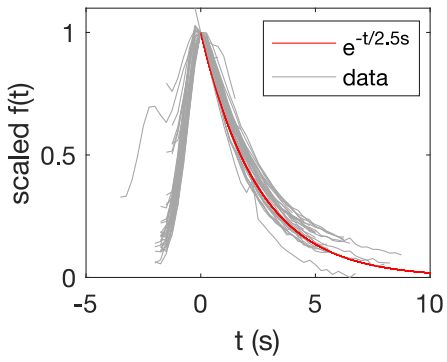

FIG. S7: Overlaid and re-scaled calcium signals from the motoneuron experiment (dataset *f1t1* from [32]) shows the decay can be well approximated by an exponential function with time constant $\tau_{ca} = 2.5$s.

bioRxiv preprint doi: https://doi.org/10.1101/2022.06.27.497721; this version posted June 29, 2022. The copyright holder for this preprint (which was not certified by peer review) is the author/funder. All rights reserved. No reuse allowed without permission.

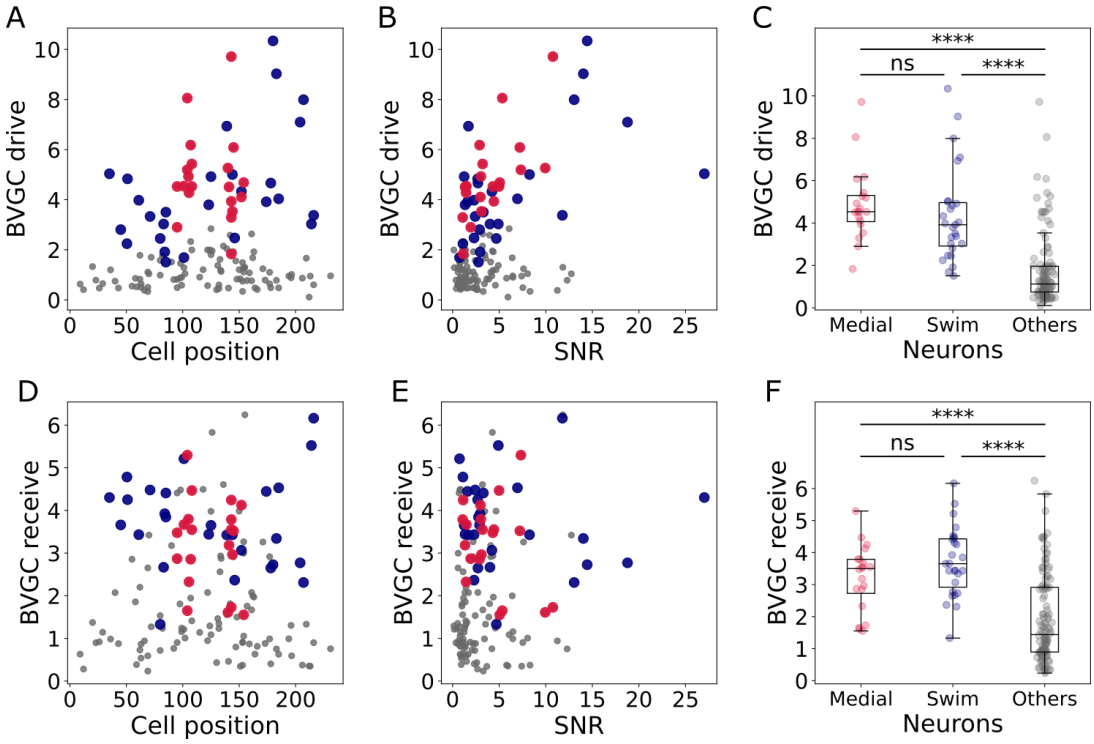

FIG. S8: Correlation of the drive and receiving values to the cell position and signal-to-noise ratio and comparison across neuron groups. (A) The neuronal drive, calculated as the sum of the strength of all outgoing Granger causality (GC) links for each neuron, is not correlated to the neuron position. In data recorded by a two-photon laser scanning microscope, different pixels are scanned across the sample with a very small delay. Panel A shows that the scanning direction and delay do not influence the GC results. (B) The neuronal drive is correlated to the signal-to-noise ratio (SNR) of the calcium traces. It is especially high for medial neurons (in red, r = 0.69 compared to r = 0.45 across all 139 neurons). After computing the new threshold for significance with a corrected null hypothesis and the normalized GC values, the correlation between the drive and SNR decreased. (C) The neuronal drive is significantly higher for motor-correlated neurons than for other neurons. This observation suggests that motor-correlated neurons are important drivers of the network activity. (D) The receiving value of a given neuron is defined as the sum of all its incoming GC links. As for the drive, it is not correlated to the cell position. (E) The receiving value is correlated to the SNR. This correlation is reduced when computing the receiving value using the normalized GC values. (F) The receiving value is significantly higher for motor-correlated than for other neurons. This shows strong information flow between the motor-correlated neurons.

bioRxiv preprint doi: https://doi.org/10.1101/2022.06.27.497721; this version posted June 29, 2022. The copyright holder for this preprint (which was not certified by peer review) is the author/funder. All rights reserved. No reuse allowed without permission.

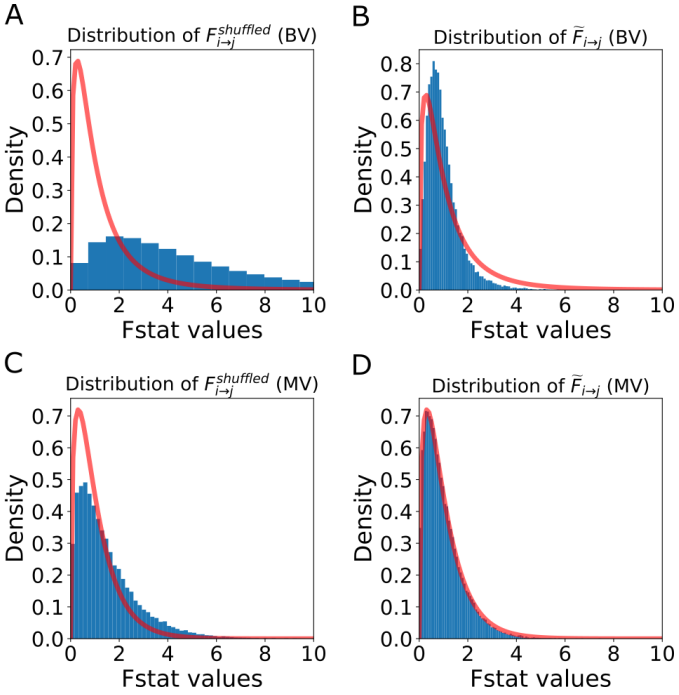

FIG. S9: Distribution of the F-statistics of the shuffled data before and after re-scaling. (A) Original distribution of the BVGC F-statistics of shuffled data $\mathcal{F}_{i\to j}^{\text{shuffled}}$. It has a shifted support that is larger than that of the F-distribution (red curve), meaning that if we use the original F-test based on the F-distribution as a null model, even if there are no Granger-causal links between two neurons, we will classify the link as significant. (B) For each neuron pair (i, j), the distribution $\mathcal{F}_{i\to j}^{\text{shuffled}}$ is well-described by a constant-rescaled F-distribution. Applying an adaptive threshold on $F_{i\to j}$ can be simplified to applying the original threshold on the normalized $\widetilde{F}_{i\to j}$, defined by dividing the naive F-statistics with the expectation value of the F-statistics generated by the shuffled data ($\widetilde{F}_{i\to j} = F_{i\to j}/\langle F_{i\to j}^{\text{shuffled}}\rangle$). (C) Original distribution of the MVGC $\mathcal{F}_{i\to j}^{\text{shuffled}}$. (D) The normalized $\mathcal{F}_{i\to j}^{\text{shuffled}}$ is almost perfectly described by a constant-rescaled F-distribution.